UNIVERSITÀ
DI PAVIA

Dipartimento di Chimica

Direttore Ch.ma Prof. Antonella Profumo

Corso di Laurea Magistrale in Chimica

Efficient and Stable $FAPbI_3$-Based Semi-transparent Perovskite Solar Cells

Relatore:
Ch.ma Prof.ssa Giulia Grancini

Correlatore:
Matteo Degani

Tesi di Laurea Magistrale di
Roberto Bigoni

Anno Accademico 2024 / 2025

Index

Riassunto

La crisi energetica e climatica ha intensificato la ricerca di fonti energetiche pulite e sostenibili. La domanda energetica globale è destinata ad aumentare considerevolmente nei prossimi decenni.[1-4] Tra le fonti energetiche rinnovabili (solare, idroelettrica, geotermica, biomasse ed eolica), l'energia solare si distingue come una delle opzioni più abbondanti e sostenibili disponibili a livello mondiale. L'energia solare rappresenta attualmente una quota significativa della capacità totale installata di energia rinnovabile. Attualmente il fotovoltaico basato sul silicio cristallino domina il mercato, principalmente grazie alla continua riduzione dei costi di produzione e dei materiali, nonché all'elevata durabilità dei dispositivi. Tuttavia, i moduli fotovoltaici in silicio cristallino presentano *energy payback times* relativamente lunghi (più di 2 anni).[8] In risposta alla domanda di tecnologie di nuova generazione, sono stati dedicati notevoli sforzi di ricerca allo sviluppo di soluzioni innovative capaci di soddisfare il cosiddetto "triangolo d'oro" dei requisiti: basso costo, alta efficienza e stabilità a lungo termine. Attualmente, le principali alternative al fotovoltaico basato sul silicio includono celle solari CIGS (seleniuro di rame indio gallio), CdTe (telloruro di cadmio), fotovoltaico organico (OPV), *dye-sensitized solar cell* (DSSC) e celle solari a perovskite (PSC). Tra le tecnologie fotovoltaiche emergenti, le celle solari a perovskite spiccano per i bassi costi di fabbricazione e per le elevate efficienze di conversione fotovoltaica. Le celle solari a perovskite (PSC) sono dispositivi fotovoltaici costituiti da un materiale attivo semiconduttore, la perovskite, interfacciato con strati di estrazione selettiva delle cariche: lo strato trasportatore di lacune (HTL) e lo strato trasportatore di elettroni (ETL) (Figura 1a). Quando i fotoni della luce visibile raggiungono la cella solare, gli elettroni nella perovskite vengono foto-eccitati verso la banda di conduzione (CB), lasciando lacune nella banda di valenza (VB), a condizione che i fotoni possiedano energia hν sufficiente (ovvero, maggiore dell'energia tra CB e VB) (Figura 1b). Per generare l'effetto fotovoltaico, la coppia elettrone-lacuna deve separarsi e le cariche opposte devono raggiungere gli elettrodi, che

tipicamente consistono in un contatto metallico e in un ossido conduttivo trasparente (TCO).[52,53]

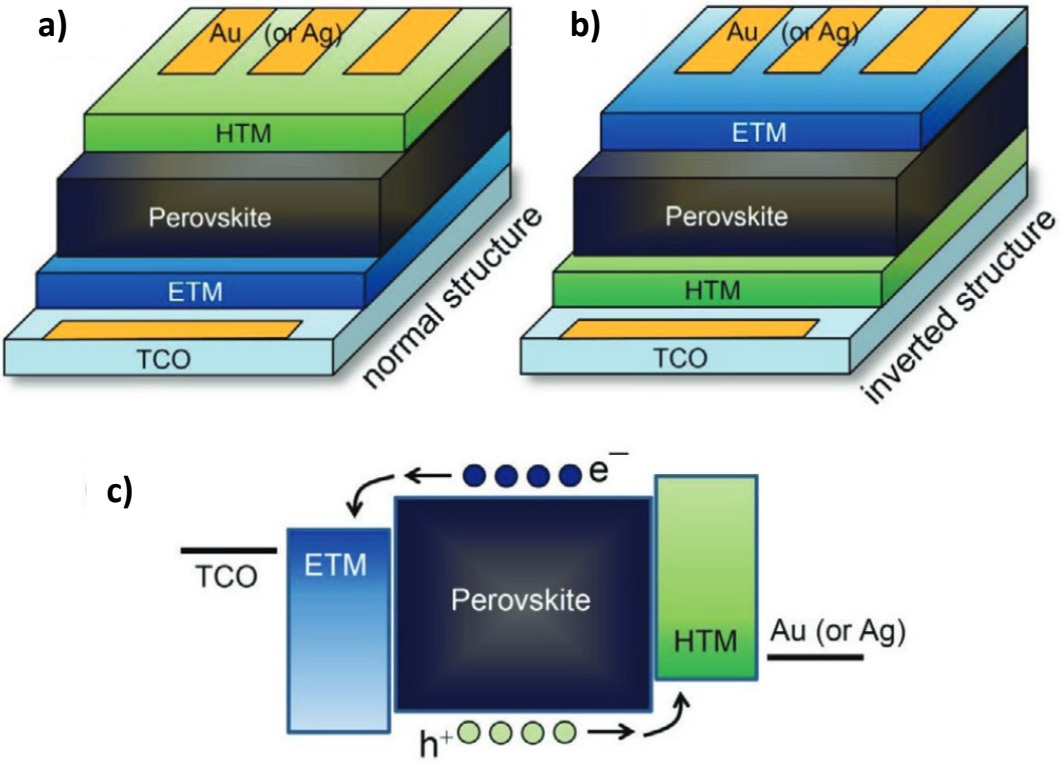

Figura 1. Architetture delle celle solari a perovskite: **a)** struttura regolare n-i-p, **b)** struttura invertita p-i-n. **c)** Diagramma dei livelli energetici che mostra il trasporto dei portatori di carica.[52]

Il termine perovskite si riferisce a un'ampia classe di materiali cristallini con formula chimica generale ABX_3, il cui nome deriva dal minerale $CaTiO_3$. All'interno di questa famiglia, le perovskiti alogenure metalliche (MHP), dove X rappresenta un anione alogenuro (Cl^-, Br^- o I^-), hanno attirato particolare attenzione per le loro eccezionali proprietà optoelettroniche. Il catione A può essere uno ione inorganico (Cs^+, Rb^+), oppure organico (Formamidinio, Metilammonio). Il sito B è tipicamente occupato da un catione metallico bivalente (Pb^{2+}, Sn^{2+}).

La struttura ideale presenta simmetria cubica, con gli anioni X posizionati al centro delle facce, il catione B al centro della cella unitaria e i cationi A agli spigoli.[45-47]

Le principali caratteristiche delle perovskiti includono:

- Bandgap diretto dovuto alla struttura cristallina altamente simmetrica;
- Elevato coefficiente di assorbimento con soglia di assorbimento netta;
- Tolleranza ai difetti, ovvero bassa tendenza a formare difetti profondi;
- Bassi tassi di ricombinazione mediati da difetti;
- Mobilità dei portatori relativamente elevate;
- Lunghe lunghezze di diffusione dei portatori (superiori a 1 μm);
- Tempi di vita dei portatori estesi (centinaia di nanosecondi);
- Ampio *tuning* del bandgap attraverso ingegneria composizionale.[48-51]

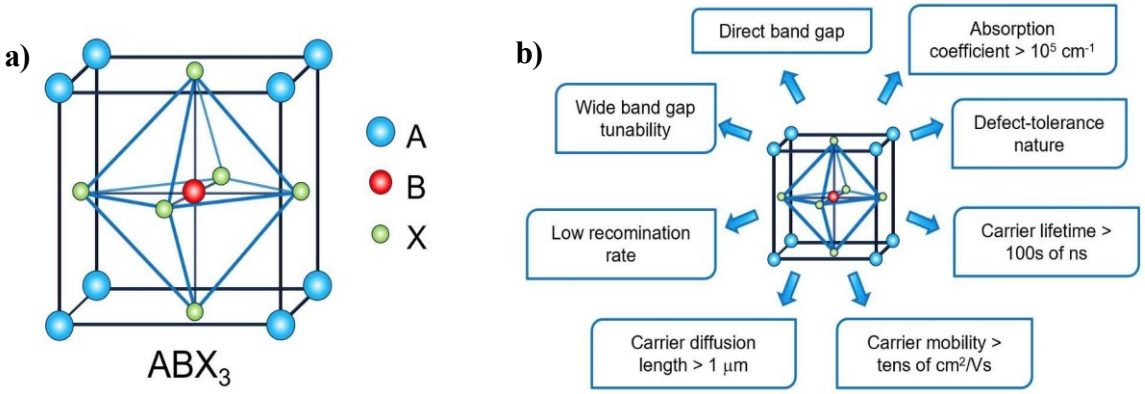

Figura 2. a) Struttura perovskite 3D. **b)** Principali proprietà optoelettroniche delle perovskiti.[51]

Nell'ultimo decennio, le celle solari a perovskite hanno raggiunto progressi notevoli, con efficienze di conversione che sono passate dal 3,8% nel 2009 a un record del 27%. Oltre alle eccezionali proprietà optoelettroniche, le perovskiti offrono due ulteriori vantaggi:

- Processabilità in soluzione a temperature relativamente basse, con *energy payback time* inferiore a un anno;
- Compatibilità con substrati flessibili.

I fotovoltaici semitrasparenti (ST-PV) sono una classe emergente di dispositivi solari progettati per generare elettricità permettendo simultaneamente la trasmissione parziale della luce visibile. Grazie alle proprietà ottiche ed elettroniche sintonizzabili di materiali come le perovskiti, gli ST-PV possono

essere personalizzati in termini di trasparenza, neutralità cromatica ed efficienza, rendendoli promettenti per applicazioni come il fotovoltaico integrato negli edifici (BIPV), serre e altri contesti dove estetica, comfort visivo e raccolta di energia devono essere combinati nello stesso dispositivo.

Oltre ai parametri fotovoltaici standard, le celle solari semitrasparenti (ST-SC) richiedono la valutazione delle proprietà ottiche. Tra queste, due parametri si distinguono come indicatori chiave di prestazione: la *average visible transmittance* (AVT) e la *light utilization efficiency* (LUE). L'AVT quantifica la frazione di luce visibile trasmessa attraverso la cella solare, ponderata sia dalla risposta spettrale dell'occhio umano che dallo spettro solare standard. Fornisce una metrica oggettiva della trasparenza della cella. La LUE è il prodotto tra AVT ed efficienza della cella solare e consente il confronto diretto tra diverse tecnologie semitrasparenti.[54,55]

Negli ultimi anni, le celle solari a perovskite sono diventate un importante focus di ricerca nel campo del fotovoltaico semitrasparente.

La semitrasparenza può essere ottenuta tramite tecniche di *patterning*, dove lo strato di perovskite viene depositato in modo spazialmente selettivo piuttosto che come film uniforme, creando regioni opache separate lateralmente da aree trasparenti.[61-63]

La modulazione della porosità viene tipicamente ottenuta riducendo la copertura superficiale attraverso trattamenti idrofobici del substrato, modificando la morfologia del film per migliorare la trasparenza mantenendo le prestazioni fotovoltaiche.[64,65]

Il controllo dello spessore può essere ottenuto regolando la concentrazione molare della soluzione precursore, con strati sottili di perovskite spesso fabbricati mediante spin-coating di soluzioni a bassa concentrazione. In alternativa, il controllo può essere ottenuto modificando i parametri di deposizione e i protocolli di ricottura. La capacità di ridurre lo spessore della perovskite senza compromettere le prestazioni deriva dal suo elevato coefficiente di assorbimento ottico, che consente un efficiente assorbimento dei fotoni anche con film ridotti, permettendo un favorevole bilanciamento tra AVT e PCE.[66-70]

Senza modificare lo spessore della perovskite, la trasparenza può essere ottenuta utilizzando perovskiti a bandgap più ampio con maggiore trasmittanza della luce visibile. Il bandgap delle perovskiti può essere efficacemente modificato sostituendo l'anione alogenuro nel sito X. Ad esempio, $CsPbBr_xI_{3-x}$, $MAPbBr_xI_{3-x}$ e $FAPbBr_xI_{3-x}$ presentano bandgap che variano rispettivamente da circa 1,73 a 2,38 eV, 1,59 a 2,30 eV e 1,48 a 2,30 eV.[71,72] Esiste un limite di miscibilità per contenuti di Br superiori a ~40%, oltre il quale le perovskiti miste ricche di bromuro subiscono severa foto-instabilità e separazione di fase. Per mitigare questo problema nelle composizioni miste Br/I, la sostituzione parziale di FA con Cs si è dimostrata una strategia efficace, producendo perovskiti ibride stabili.[73,74]

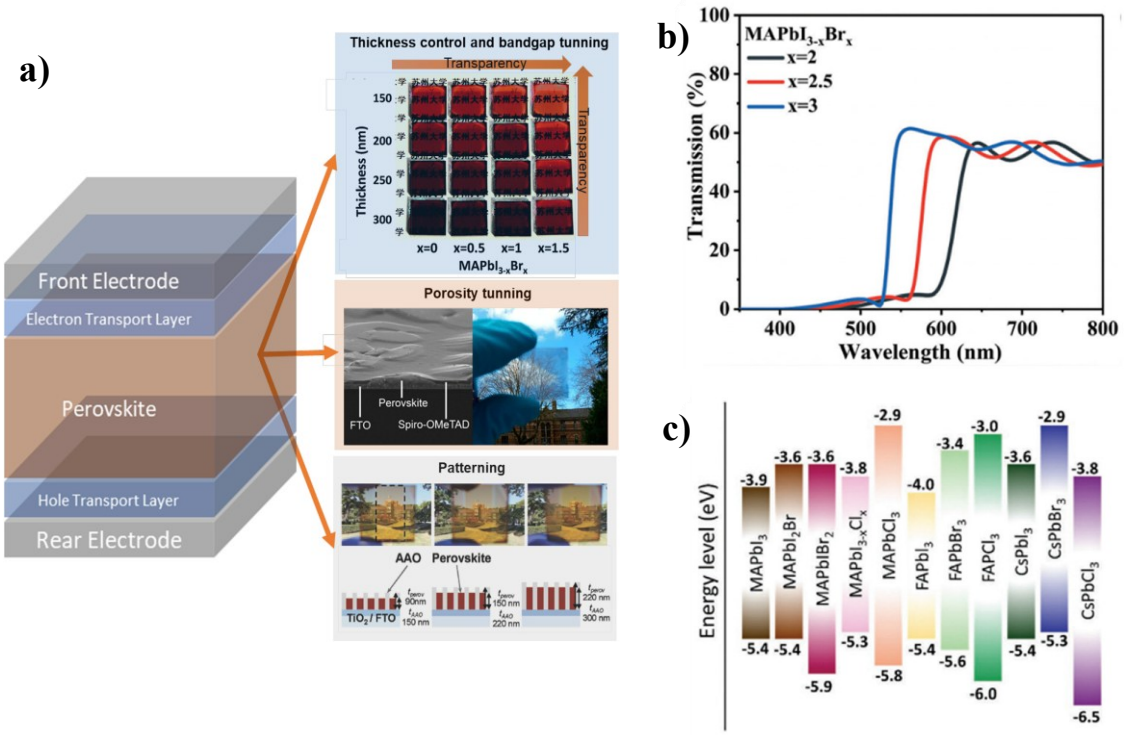

Figura 3. a) Strategie per fabbricare celle solari seitrasparenti a perovskite.[101] **b)** Spettri di trasmittanza di perovskiti con diverse quantità di bromo.[55] **c)** Livelli energetici di perovskiti con diverso bandgap.[102]

Le perovskiti a bassa dimensionalità (LD-HP) rappresentano una strategia promettente per migliorare la stabilità rispetto alle perovskiti 3D, sebbene con prestazioni optoelettroniche generalmente inferiori. Questi materiali si formano intercalando cationi organici ingombranti tra gli strati ottaedrici inorganici, creando strutture bidimensionali. Le LD-HP più comuni sono le perovskiti Ruddlesden-Popper (RP), dove R è un catione monoamminico, mentre l'uso di cationi diamminici dà origine alle fasi Dion-Jacobson (DJ). Il numero di strati inorganici tra i distanziatori organici è indicato con n. Per n = 1 si ottiene una perovskite 2D pura, mentre nel limite n→∞ la struttura si avvicina a una perovskite 3D. Le perovskiti quasi-2D corrispondono tipicamente a valori di n tra 2 e 5-6 (**Figura 4a)**. All'aumentare del numero di strati inorganici, sia il bandgap che l'energia di legame dell'eccitone diminuiscono, rendendo le perovskiti quasi-2D un'alternativa adatta alle controparti 3D a bandgap largo per applicazioni fotovoltaiche semitrasparenti (**Figura 4b**). Tuttavia, gli strati organici isolanti ostacolano il trasporto di carica, rendendo necessario il controllo dell'allineamento verticale degli strati inorganici per migliorare l'estrazione dei portatori e le prestazioni del dispositivo.[75-78]

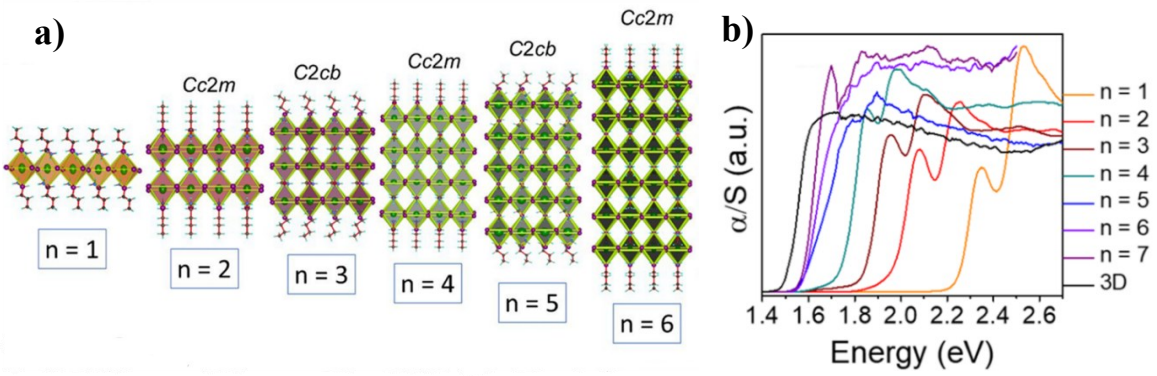

Figure 1. a) Struttura cristallina e **b)** spettri di assorbimento di perovskiti quasi-2D con diversi valori di *n*.[77]

In questo lavoro, introduciamo una strategia alternativa alle perovskiti ad ampio bandgap basata su ioduro di piombo e formamidinio ($FAPbI_3$), un materiale a basso bandgap tipicamente impiegato in celle solari opache. Attraverso un'ingegnerizzazione precisa dello strato assorbitore di $FAPbI_3$, presentiamo dispositivi che offrono simultaneamente elevata trasparenza ottica ed efficienza di conversione competitiva. Per le celle solari è stata scelta l'architettura inversa *p-i-n.* Un elettrodo trasparente di ossido di indio-stagno (ITO) e un film sottile di argento (Ag) sono stati impiegati come contatti elettrici delle celle solari. Come strati trasportatori di carica sono stati utilizzati l'acido fosfonico 2-(3,6-dimetossi-9H-carbazolo)etile (MeO-2PACz) per l'HTL e l'estere metilico dell'acido [6,6]-fenil-C_{61}-butirrico (PCBM) per l'ETL. Infine, uno strato di batocuproina (BCP) è stato depositato come strato buffer per bloccare il trasporto delle lacune verso il catodo e prevenire la diffusione dell'argento all'interno del dispositivo

Lo spessore dello strato di perovskite è stato controllato variando le concentrazioni dei precursori in soluzione. Tra le diverse concentrazioni investigate, le formulazioni 0,5 M e 0,6 M hanno dimostrato prestazioni ottimali. Per quantificare l'impatto dello spessore sulla trasmissione luminosa, abbiamo misurato gli spettri di assorbimento UV-Vis dell'intera struttura del dispositivo (Vetro/ITO/MeO-2PACz/$FAPbI_3$/PCBM/BCP) escludendo il contatto metallico.

I valori di AVT, calcolati utilizzando l'Equazione 7, sono risultati del 24,2% e 18,2% rispettivamente per le concentrazioni di precursori 0,5 M e 0,6 M. Mezze celle (Vetro/ITO/MeO-2PACz/Perovskite) sono state caratterizzate mediante microscopia elettronica a scansione a emissione di campo (FESEM) per determinare gli spessori dello strato di perovskite (Figura 21 a,b). Le misurazioni hanno fornito intervalli di spessore di 130-150 nm per la concentrazione di precursori 0,5 M e 150-170 nm per 0,6 M.

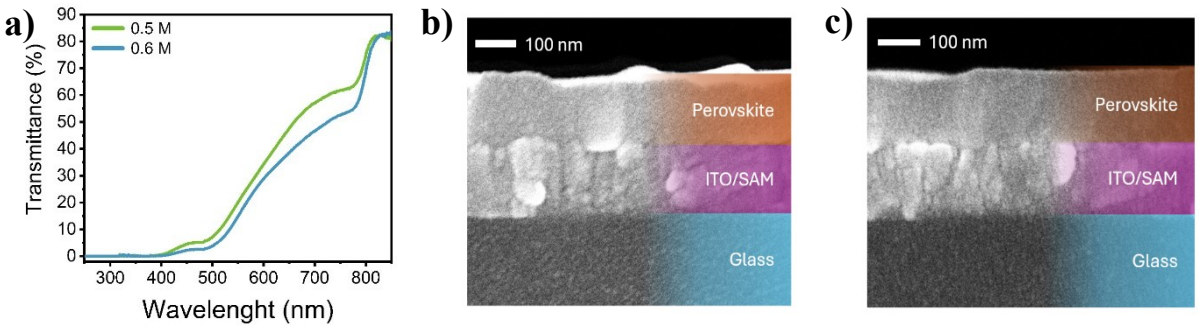

Figura 5. a) Spettri di trasmittanza per diverse concentrazioni di perovskite. Immagini SEM *cross section* di strati di perovskite con concentrazioni di precursori di **b)** 0.5 M e **c)** 0.6 M.

Le prestazioni dei dispositivi sono state valutate misurando i parametri fotovoltaici sotto illuminazione standard AM 1.5G. Il dispositivo migliore da 140 nm ha raggiunto una densità di corrente di cortocircuito (J_{SC}) di 19 mA·cm^{-2}, una tensione di circuito aperto (V_{OC}) di 998 mV, un *fill factor* (FF) dell'83,4%, risultando in un'efficienza di conversione (PCE) del 15,9%. Il dispositivo da 160 nm ha fornito prestazioni superiori con J_{SC} di 20,9 mA·cm^{-2}, V_{OC} di 1031 mV, FF dell'83,7% e PCE del 18%. Nonostante i promettenti valori di J_{SC} e AVT, i dispositivi hanno mostrato una V_{OC} relativamente bassa, limitando quindi la PCE complessiva. Per affrontare questo problema, sono state impiegate tecniche di passivazione superficiale. Tra tutti gli agenti passivanti valutati, FPEAI 5 mM in CB/IPA 9:1 ha fornito i risultati più promettenti. D'ora in avanti, i dispositivi passivati saranno indicati come 140 nm FPEAI e 160 nm FPEAI. La **Figura 6** mostra il confronto tra i dispositivi passivati e non passivati. Il dispositivo passivato da 140 nm ha dimostrato parametri migliorati con V_{OC} di 1144 mV, J_{SC} di 18,2 mA·cm^{-2}, FF dell'81,9%, risultando in una PCE del 17,0%. Analogamente, il dispositivo passivato da 160 nm ha raggiunto V_{OC} di 1145 mV, J_{SC} di 20,6 mA·cm^{-2}, FF dell'82,9% e PCE del 19,5%. Questi miglioramenti convalidano l'efficacia della strategia di passivazione superficiale con FPEAI nel migliorare le prestazioni del dispositivo senza compromettere la trasparenza.

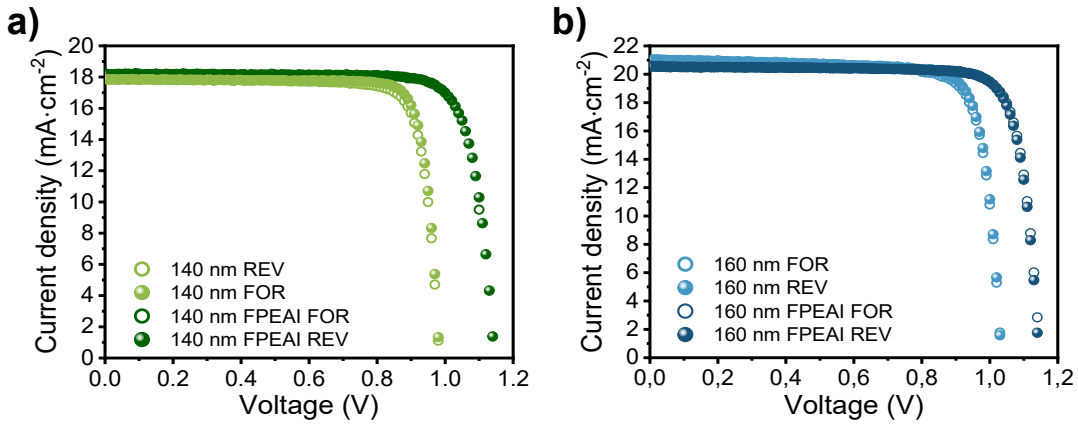

Figura 7. Curve J−V dei dispositivi passivati e non passivati con spettro solare AM1.5G.

Studi di fotoluminescenza (PL) e fotoluminescenza risolta nel tempo (TRPL) sono state eseguite per investigare i meccanismi sottostanti responsabili del miglioramento delle prestazioni fotovoltaiche osservato nei dispositivi passivati. I film di perovskite passivati mostrano un'intensità di emissione PL aumentata rispetto alle controparti non passivate per entrambi gli spessori (**Figura 8**). Il segnale PL incrementato indica una qualità superficiale migliorata e perdite non radiative associate agli stati di trappola superficiali soppresse.

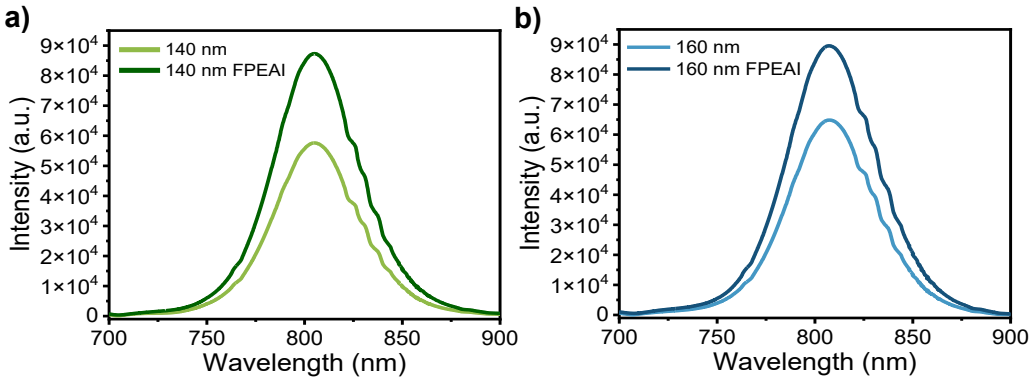

Figura 8. Spettri di fotoluminescenza (PL) dei dispositivi da **a)** 140 nm e **b)** 160 nm, prima e dopo la passivazione.

L'analisi di fotoluminescenza risolta nel tempo (TRPL) è stata eseguita per quantificare la dinamica dei portatori (**Figura 9**). I campioni trattati con FPEAI dimostrano *effective radiative lifetimes* (τ_{eff}) estesi rispetto alle controparti non passivate.[91-94]

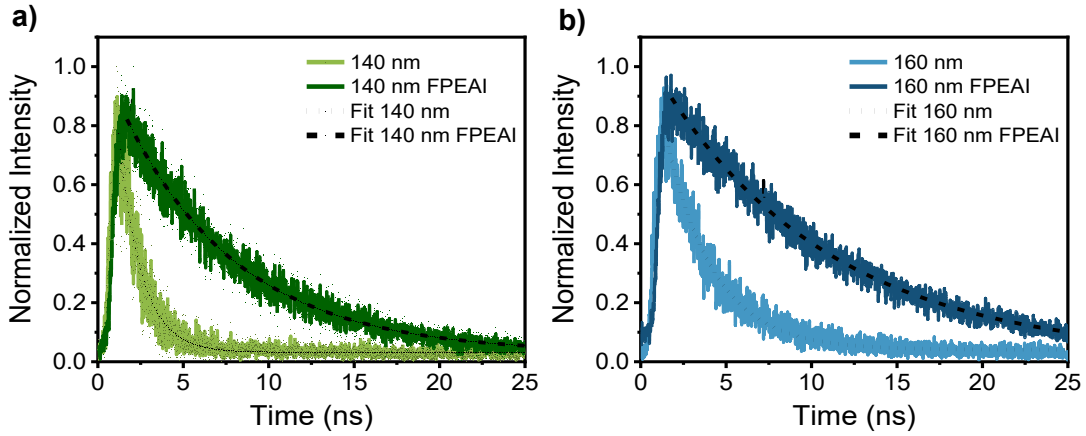

Figura 9. Time-resolved photoluminescence (TRPL) dei dispositivi da **a)** 140 nm e **b)** 160 nm, prima e dopo la passivazione.

Maximum power point (MPP) *stability tests* sono stati condotti per valutare la stabilità operativa dei dispositivi non passivati. I risultati presentati in **Figura 10** dimostrano che entrambi gli spessori hanno superato la soglia di ritenzione dell'80% dopo 1000 ore di illuminazione continua. I dispositivi da 140 nm hanno mantenuto l'88%, mentre i dispositivi da 160 nm hanno mantenuti l'83% delle loro efficienze iniziali.

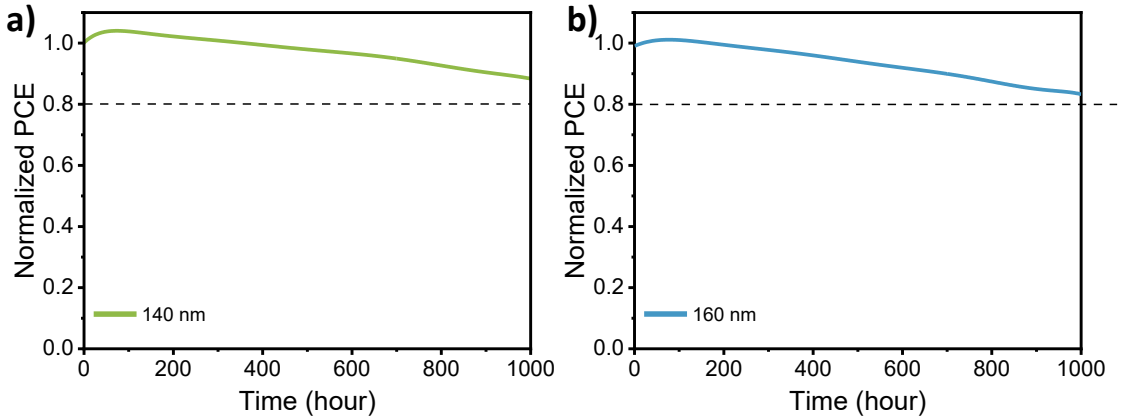

Figura 10. *MPP tracking stability test* dei dispositivi da **a)** 140 nm e **b)** 160 nm. La linea tratteggiata rappresenta l'80% della PCE iniziale.

In conclusione l'ottimizzazione dello spessore di $FAPbI_3$ e la passivazione superficiale hanno permesso di ottenere celle solari con ottimo equilibrio tra trasparenza ed efficienza, prestazioni avanzate e alta stabilità.

Chapter 1
Introduction

1.1 Energy Problem

The ongoing energy and climate crisis has intensified the search for new clean and sustainable energy sources.[1–3] Fossil fuels, long considered the backbone of modernization, are now being reassessed because of their non-renewable characteristics, and significant greenhouse gasses emission. International Energy Agency (IEA)'s 2024 report stated that the global final energy consumption currently stands at 445 exajoules (1 EJ = 10^{18} J). In the Stated Policies Scenario (STEPS), this rises steadily to over 530 EJ by 2050.[4] Solar, hydropower, geothermal, biomass, and wind energy sources have been widely studied as alternatives to fossil fuels. Among these, solar energy stands out as one of the most abundant and sustainable options available worldwide.[5] Thus, the net energy of solar irradiation reaching Earth is calculated as $1.73 \cdot 10^{17}$ Watts. Therefore, the net solar energy reaching Earth annually is $5.4 \cdot 10^{6}$ EJ, which is 10000 higher than the current annual energy demand of Earth.[6] Currently, solar energy accounts for 41% of the total installed renewable energy capacity, with a total of 1866 GW in 2024 (**Figure 1**).[7]

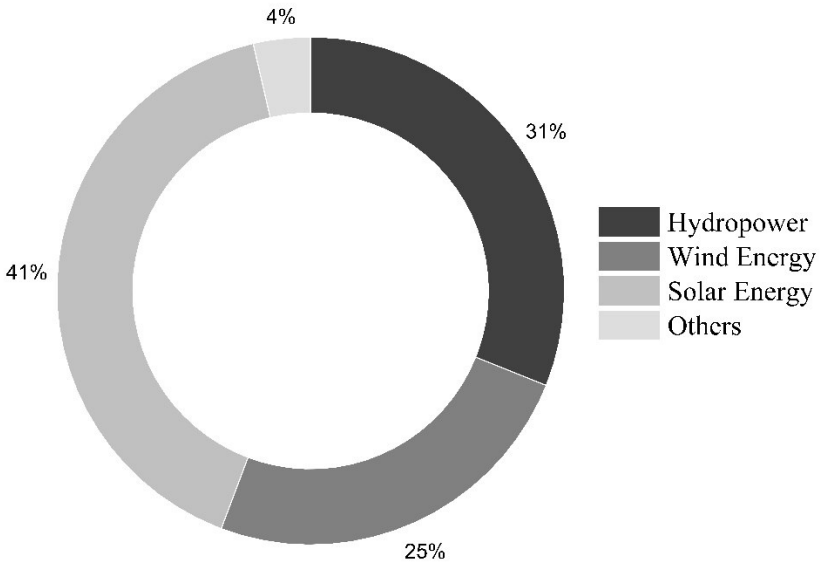

Figure 2. Renewable power capacity by energy sources at the end of 2024.[6]

Currently, crystalline-silicon-based photovoltaic (c-Si PV) technology dominates the solar energy market, primarily due to the continuous decline in manufacturing and material costs as well as the high durability of the devices. However, c-Si PV modules have an energy payback (EPBT) time of almost 2 years.[8]

1.2 Solar Photovoltaics

Working principles

The operation of solar cells is based on the photovoltaic effect, namely the generation of a potential difference at the junction of two different materials in response to electromagnetic radiation. In general, any material can absorb photons with energy hν (where h is Planck's constant and ν is the frequency) if this energy is equal to or greater than the difference between the lowest unoccupied and the highest occupied electron energy levels. In crystalline solids, such as inorganic semiconductors, this energy difference is called the bandgap (E_g), which corresponds to the separation between the conduction band edge (E_C) and the valence band edge (E_V). If the photon energy is smaller than the bandgap, it cannot be absorbed. When excitation occurs, the electron is promoted to the conduction band, leaving behind a vacancy in the valence band. This vacancy behaves as a positively charged quasiparticle, known as a hole, so that photon absorption ultimately results in the generation of an electron–hole pair (**Figure 2a**). A solar cell must be designed so that photogenerated electrons and holes reach the electrodes before recombining, meaning the time required for charge carriers to travel to the contacts must be shorter than their lifetime; this requirement places an upper limit on the thickness of the absorber layer. Once excited, electrons in the conduction band and holes in the valence band are mobile and can be separated, enabling their flow through an external circuit and thus producing the photovoltaic effect. To selectively extract these charge carriers, solar cells typically employ p–n junctions, where the built-in potential arising from the different work functions of the p-type and n-type regions drives the separation of electrons and holes (**Figure 2b**).[9–11]

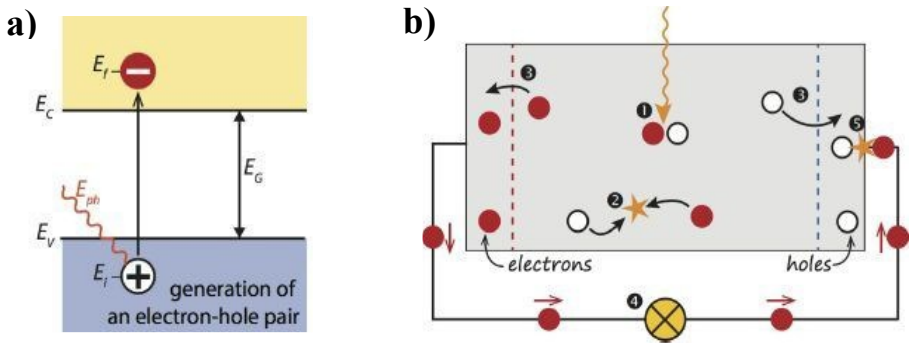

Figure 3. a) Absorption of a photon in a semiconductor with bandgap E_G. **b)** Schematic of charge carrier dynamics in a perovskite solar cell showing electrons (red), holes (white).[10]

Photovoltaic Parameters

Solar cell performance is typically assessed by applying a voltage (V) to the device and recording the corresponding current (I), thereby obtaining the current–voltage (I–V) characteristic. The equivalent (electrical) circuit-based models are most widely used to simulate PV cells. The most common and simplest approach to model I–V curves is the single-diode R_P equivalent circuit (**Figure 3a**). This model consists of:

- A current source representing the photocurrent (I_{PV});
- A p-n junction diode connected in parallel to the current generator source;
- A series resistance (R_S) accounting for resistive losses within the active materials, electrodes and interfaces;
- A shunt resistance (R_P) accounting for leakage pathways and temperature dependent losses.

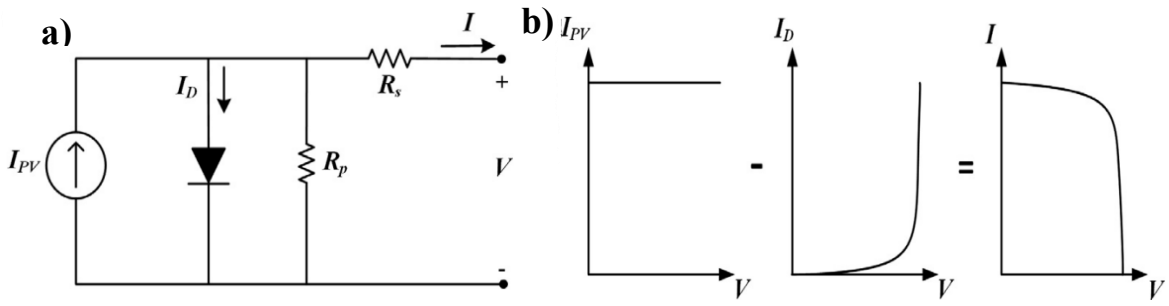

Figure 4. a) The single diode RP-model of PV cell. **b)** Superposition of I_{PV} and I_D.[12]

In the absence of solar illumination, the cell behaves as a simple p-n junction diode, and the diode current is expressed as:

$$I_D = I_0 \left[e^{\frac{q(V+IR_S)}{akT}} - 1 \right] \quad (1)$$

where I_0 is the saturation current, q is the elementary charge (-1,60217646 × 10^{-19} C), a is the ideality factor, k is the Boltzmann's constant (-1.380653 × 10^{-19} J/K), and T is the junction temperature (K).

Upon exposure to light, incident photons are absorbed by the p-n junction, generating electron-hole pairs. The cells' output current is given by the following equation:

$$I = I_{PV} - I_D - I_{R_P} = I_{PV} - I_0 \left[e^{\frac{q(V+IR_S)}{akT}} - 1 \right] - \frac{V + IR_S}{R_p} \quad (2)$$

As shown in equation 2, the current output of a solar cell results from the superposition of the photocurrent (I_{PV}) and the diode dark current (I_D), as illustrated in **Figure 3b**.[11–14]

The key parameters describing solar cell performance are the maximum power point (MPP), the short circuit current density (J_{SC}), the open circuit voltage (V_{OC}), the fill factor (FF), and the power conversion efficiency (PCE).

- The short-circuit current (I_{SC}) corresponds to the current flowing through the external circuit when the solar cell is short-circuited. Since I_{SC} scales with the cell area, the short-circuit current density (J_{SC}) is generally used for device comparison, as it provides a normalized measure of the maximum current a solar cell can deliver. The magnitude of J_{SC} is strongly influenced by the optical properties of the device, such as light absorption and reflection.
- The open-circuit voltage (V_{OC}) is defined as the voltage across the terminals of the solar cell when no external current is drawn. It corresponds to the maximum voltage the device can provide under illumination and is strongly influenced by recombination processes within

the absorber and at the interfaces. Hence, V_{OC} serves as a key indicator of the extent of carrier recombination in the device.

- The maximum power point (MPP) is the point on the J-V curve at which the device solar cell delivers its highest maximal power output (**Figure 4a)**.
- The fill factor (FF) is defined as the ratio between the maximum power output ($P_{MP} = J_{MP} \cdot V_{MP}$) and the product of the open-circuit voltage (V_{OC}) with the short-circuit current density (J_{SC}). Graphically, it corresponds to the ratio between the area of the grey rectangle and that of the light-blue rectangle (**Figure 4b**).

$$FF = \frac{V_{MP} \cdot J_{MP}}{V_{OC} \cdot J_{SC}} \tag{3}$$

- Power conversion efficiency (PCE) is defined as the fraction of incident power converted to electricity:

$$PCE = \frac{V_{OC} \cdot J_{SC} \cdot FF}{P_{in}} \tag{4}$$

Where P_{in} is the Power of the incident radiation.[10,15]

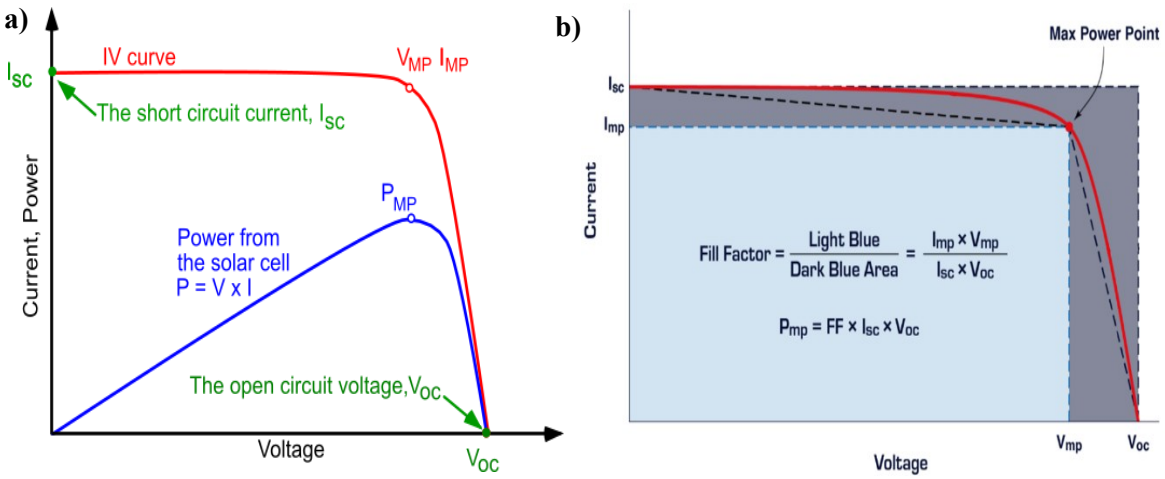

Figure 5. a) Typical current-voltage (J-V) characteristics of a solar cell showing short-circuit current (Jsc), open-circuit voltage (Voc and maximum power point (MPP).[15] **b)** Graphical representation of fill factor (FF) calculation from the J-V curve.[99]

Solar Spectra

The surface temperature of the Sun is approximately 6000 K. If it was a perfect blackbody, its emission spectrum would correspond to that shown in **Figure 5**. However, the actual spectrum measured outside the Earth's atmosphere differs and is referred to as the AM0 spectrum, with a solar irradiance of about 1361 W/m². As sunlight passes through the atmosphere, it becomes attenuated. The key parameter determining the level of attenuation is the distance that the radiation must travel through the atmosphere. The ratio between the actual path length of sunlight and the shortest possible path (Zenith) is known as the optical air mass (AM). When the sun is at an angle θ with the zenith, the air mass is given by:

$$\mathrm{AM} = \frac{1}{\cos\theta} \tag{5}$$

The attenuation of solar radiation is primarily caused by scattering and absorption due to air molecules, dust particles, and aerosols present in the atmosphere. In particular, water vapor (H_2O), oxygen (O_2), carbon dioxide (CO_2), and ozone (O_3) contribute to absorption. Because this absorption is wavelength-selective, it produces characteristic gaps in the solar spectral distribution, as illustrated in **Figure 5**. To allow consistent comparison of solar cells and PV modules, standard test conditions (STC) are defined. These conditions correspond to an irradiance of 1000 W/m², an AM1.5 spectrum, and a cell temperature of 25 °C. The AM1.5 spectrum corresponds to a solar zenith angle around 48.2°.[10,11]

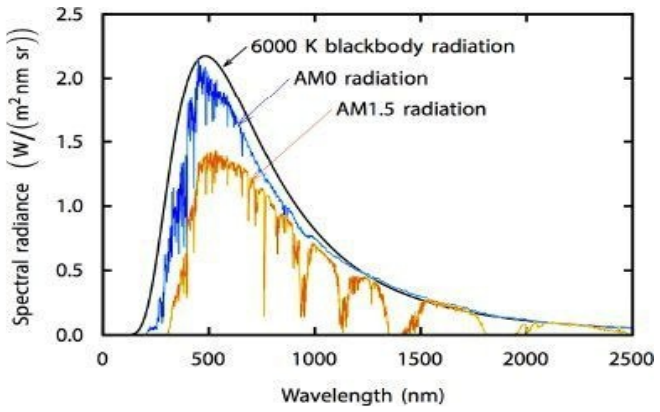

Figure 6. Different solar spectra: the blackbody spectrum of a blackbody at 6,000 K, the extraterrestrial AM0 spectrum and the AM1.5 spectrum.[10]

Schockley-Queisser limit

In 1961, William Shockley and Hans J. Queisser calculated the theoretical limit for single-junction solar cells based solely on physical principles, without relying on empirically determined constants. Their analysis was based on the following assumptions:

- The solar spectrum is approximated as blackbody radiation with a surface temperature of 6000 K;
- The solar cell is at a temperature of 300 K;
- Complete absorption of all photons with energy above the bandgap, with no interaction for photons with energy below the bandgap;
- Infinite carrier mobility, allowing full collection regardless of where carriers are generated;
- Radiative recombination is the only possible recombination mechanism.

With these assumptions, they calculated a maximum efficiency of 30% for a bandgap of 1.1 electronvolts (eV). More recently, updated Shockley–Queisser limits have been determined using the AM1.5G solar spectrum. Based on this spectrum, the calculated maximum efficiency is 33.16%, corresponding to a semiconductor bandgap of 1.34 eV. The efficiency trends as a function of bandgap are shown in **Figure 6**.[10,16–18]

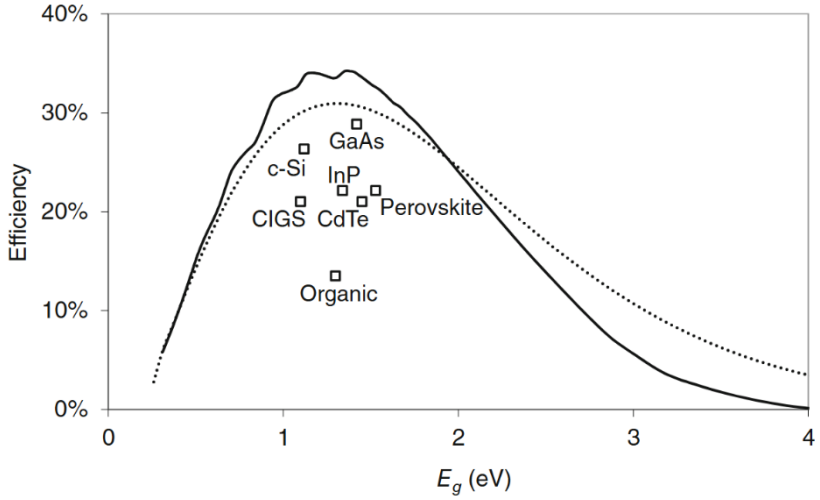

Figure 7. Theoretical one-sun efficiency limit under AM1.5 solar spectrum (solid line) compared with record device efficiencies. The SQ efficiency limit for black-body radiation is shown for reference (dotted line).[18]

1.3 Emerging Photovoltaics

As outlined in Section 1.1, among the various renewable energy sources, photovoltaic has gained significant attention in addressing the current global energy challenge. In response to the demand for next-generation technologies, commonly referred to as emerging PVs, considerable research efforts have been devoted to developing innovative solutions capable of fulfilling the so-called "golden triangle" of requirements: low cost, high efficiency, and long-term stability (**Figure 7**).

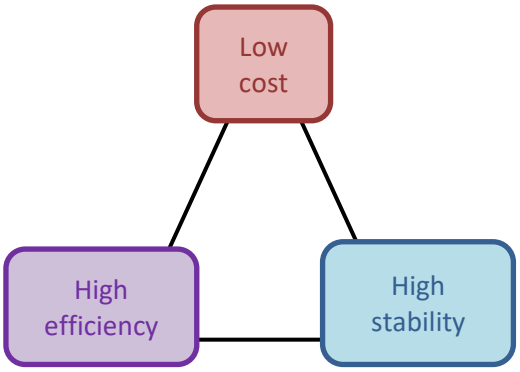

Figure 8. The three key requirements for commercial solar cell viability: low cost, high efficiency, and high stability.

Currently, the primary alternatives to silicon-based photovoltaics include copper indium gallium selenide (CIGS), cadmium telluride (CdTe), organic photovoltaics (OPV), dye-sensitized solar cells (DSSC), and perovskite solar cells.

CdTe Solar Cells

Cadmium Telluride (CdTe) is a polycrystalline thin-film semiconductor with an ideal direct bandgap of 1.45 eV, which closely matches the maximum of the solar spectrum and corresponds to a theoretical efficiency limit of approximately 32%. CdTe solar cells are widely recognized for their low fabrication costs, high power conversion efficiency, and excellent chemical stability. CdTe thin-film cells possess a simple device structure (**Figure 8**) composed of:

- Front contact (substrate + transparent conductive oxide + high resistance

transparent layer): allows light to enter while collecting electrons.

- Buffer layer (Cadmium Sulfide CdS): forms the p–n junction with CdTe, while still transmitting light.
- Absorber (CdTe): represents the core of the cell, where photons are absorbed and charge carriers are generated.
- Back contact (Te-rich layer + buffer + electrode): extracts holes from the CdTe layer and completes the electrical circuit.

The development of semi-transparent CdTe thin-film photovoltaics faces major challenges due to high production costs, the environmental toxicity of cadmium, and the limited availability of tellurium. Proper recycling and treatment practices are therefore essential for sustainable deployment.[19–21]

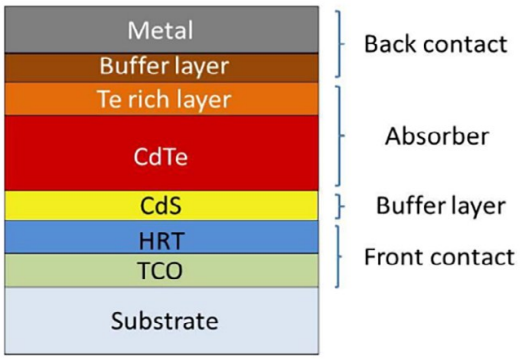

Figure 9. Device structure of CdTe solar photovoltaics. [19]

CIGS Solar Cells

Copper indium gallium selenide (CIGS) is a quaternary I–III–VI_2 compound semiconductor that has emerged as one of the most promising absorber materials for thin-film photovoltaics. Its bandgap can be tuned in the range of approximately 1.0–1.7 eV by controlling the indium-to-gallium ratio, enabling optimization of spectral utilization and device efficiency. Conventional CIGS solar cells are usually fabricated in a substrate configuration with molybdenum as the back contact, a polycrystalline CIGS absorber layer, a CdS or Cd-free buffer layer, and a transparent conductive oxide, such as aluminum-doped ZnO, as the front electrode (**Figure 9**). This architecture has resulted in record efficiencies

exceeding 23%.[22]

CIGS solar cells provide several additional advantages, including strong light-harvesting capabilities, flexibility for deposition on curved or lightweight substrates, and higher long-term stability compared to other technology. Moreover, CIGS requires fewer raw materials than crystalline silicon devices and allows for relatively cost-effective manufacturing. Nevertheless, challenges include the use of heavy metals in CIGS compositions, which raise environmental concerns and necessitate proper recycling, as well as the natural scarcity and high cost of indium and gallium.[23–26]

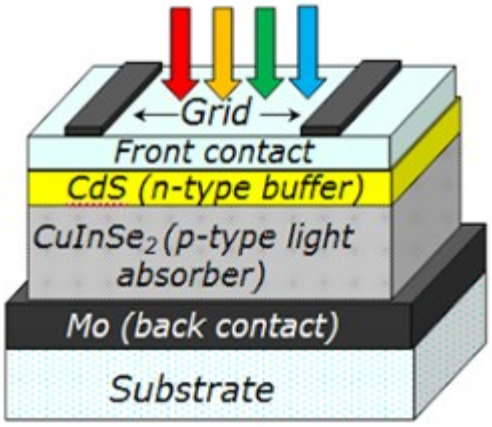

Figure 10. Device structure of a CIGS solar cell.[26]

Organic Solar Cells

Organic solar cells (OSCs) have emerged as promising photovoltaic technology due to their tunable bandgap, lightweight and flexible structure, and synthetic versatility. In addition to offering low manufacturing costs, their production generates less waste and fewer emissions compared to silicon-based devices, making OSCs an environmentally and economically sustainable alternative within thin-film photovoltaics. Early research on organic semi-transparent photovoltaics (STPVs) predominantly employed fullerene derivatives as electron acceptors. However, the power conversion efficiency (PCE) of such devices generally remained below 8%, mainly due to the limited tunability of the energy levels of fullerene derivatives and their restricted photon absorption primarily

within the visible wavelength range. In recent years, the introduction of novel and highly efficient non-fullerene acceptor materials, such as ITIC, Y6, and their respective derivatives, has paved the way for significant advancements in the field of organic PVs. The OPV device usually requires a bulk heterojunction (BHJ) which can be fabricated by mixing an electron-donor (p-type semiconductor) and electron-acceptor (n-type semiconductor). The former material involves a π-conjugated polymer and a small molecule semiconductor, and the latter material is normally a fullerene derivative (**Figure 10**). However, the pronounced sensitivity of OSCs to environmental factors such as light, humidity, and temperature results in poor operational stability, which has hindered their large-scale development and industrial maturity.[27–32]

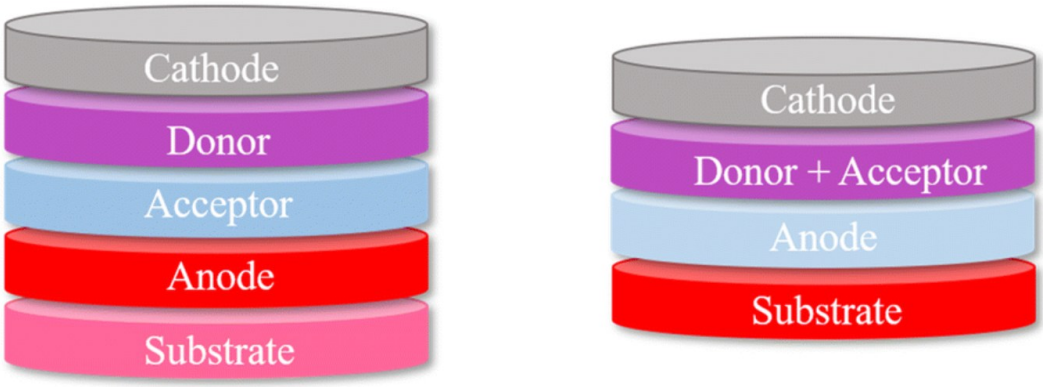

Figure 11. Structure of OSCs: **a)** double-layer heterojunction cell; **b)** bulk-heterojunction cell.[27]

Dye-Sensitized Solar Cells

Dye-sensitized solar cells (DSSCs) present several advantages, including structural simplicity, low fabrication cost, and effective power generation under low-light conditions. In addition, they exhibit high optical transmittance, strong sensitivity to diffuse illumination, and allow color tunability through the selection of different sensitizing dyes. A dye-sensitized solar cell (DSSC) is primarily composed of transparent photoanode, dye sensitizers, an electrolyte, and a counter electrode. The photoanode typically consists of a transparent conductive oxide (TCO) substrate coated with a porous semiconductor layer, commonly TiO_2 or ZnO, capable of absorbing the dye molecules that act as light-harvesting

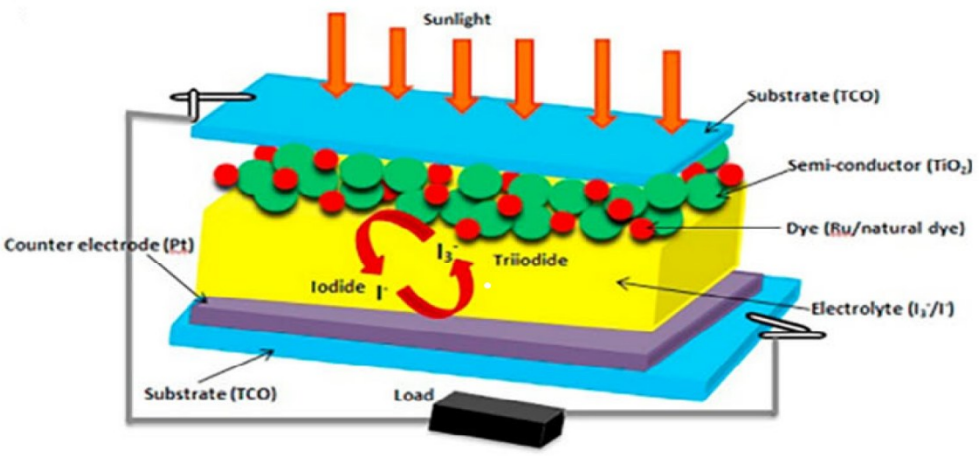

Figure 12. Schematic diagram of a dye-sensitized solar cell.[100]

sensitizers (**Figure 11**).[33–36] The dye is a key component in semi-transparent DSSCs, as it governs both transparency and absorption characteristics. Metal-based dyes, particularly ruthenium complexes, have been widely studied due to their broad absorption spectrum and effective compatibility with I^-/I_3^- electrolytes.[37–39] Despite their strong performance, ruthenium-based dyes face critical challenges, such as high cost, toxicity concerns, scarcity of ruthenium in the Earth's crust and complicated synthesis and purification procedures.[40] As alternatives, other metal-based dyes, such as those derived from titanium, vanadium, and chromium complexes, have been explored.[41,42] In parallel, organic metal-free dyes have attracted considerable attention owing to their low cost, high molar extinction coefficients, environmental compatibility, and structural flexibility, making them strong candidates for the next generation of semi-transparent DSSCs. Organic dye molecules commonly adopt a donor–π–acceptor (D–π–A) structural motif, where the donor group provides electron-rich functionality, the π-conjugated bridge facilitates charge transfer, and the acceptor group serves as the electron-withdrawing unit.[43] The main drawback of dye-sensitized solar cells (DSSCs) lies in their limited long-term stability, which significantly hinders large-scale commercialization. This instability mainly arises from the liquid electrolyte, which is prone to leakage, evaporation, and decomposition under environmental stress such as heat, moisture, and UV radiation.[44]

Perovskite Solar Cells

Structure and Properties

The term perovskite refers to a broad class of crystalline materials with the general chemical formula ABX_3. The name originates from the mineral $CaTiO_3$, first described by Gustav Rose in 1839 and later classified by the mineralogist Lev Perovski. Within this family, metal halide perovskites (MHPs), where X denotes a halide anion (Cl^-, Br^-, or I^-), have attracted particular attention due to their exceptional optoelectronic properties and their central role in perovskite solar cells (PSCs).

Depending on the chemical nature of the A-site cation, halide perovskites can be categorized into two main groups:

- Inorganic perovskites, incorporating small inorganic monovalent cations (e.g., Cs^+, Rb^+);
- Hybrid organic–inorganic perovskites, containing molecular cations such as methylammonium ($CH_3NH_3^+$) or formamidinium ($CH(NH_2)_2^+$).

The B-site is typically occupied by a divalent metal cation (Pb^{2+}, Sn^{2+}). As shown in **Figure 12a**, the ideal perovskite structure exhibits cubic symmetry, with X anions positioned at the face centers of the unit cell, the B cation located at the center, and the A cations occupying the corners. The structural stability of these materials can be semi-empirically assessed through the Goldschmidt tolerance factor (t), defined as:

$$t = \frac{r_A + r_B}{\sqrt{2}(r_B + r_X)} \tag{6}$$

where r_A, r_B, and r_X are the ionic radii of A, B, and X ions respectively. Material compositions with tolerance factors in the range $0.8 < t < 1$ can also crystallize in a cubic perovskite structure. When $t < 0.8$, less symmetric phases such as orthorhombic, rhombohedral, or ilmenite-type structures are typically formed. Conversely, values of $t > 1$ may lead either to the stabilization of hexagonal phases with face-sharing octahedra or to a destabilization of the three-

dimensional B–X framework.[45–47]

The main features of halide perovskites (HPs) can be summarized as follows:

- Direct bandgap, enabled by their highly symmetric crystal structure.
- High absorption coefficient (> 10^5 cm^{-1}) with a sharp absorption onset.
- Defect tolerance, i.e. a low tendency to form deep-level defects that would otherwise impair optical and electronic properties.
- Low defect-mediated recombination rates, thanks to their defect-tolerant nature.
- Relatively high carrier mobility, on the order of tens of $cm^2/V \cdot s$.
- Long carrier diffusion lengths, typically exceeding 1 μm.
- Extended carrier lifetimes, on the scale of several hundred nanoseconds.
- Wide bandgap tunability, achievable through compositional engineering.

These properties (summarized in **Figure 12b**) establish HPs as a leading material platform for next-generation PV technologies.[48–51]

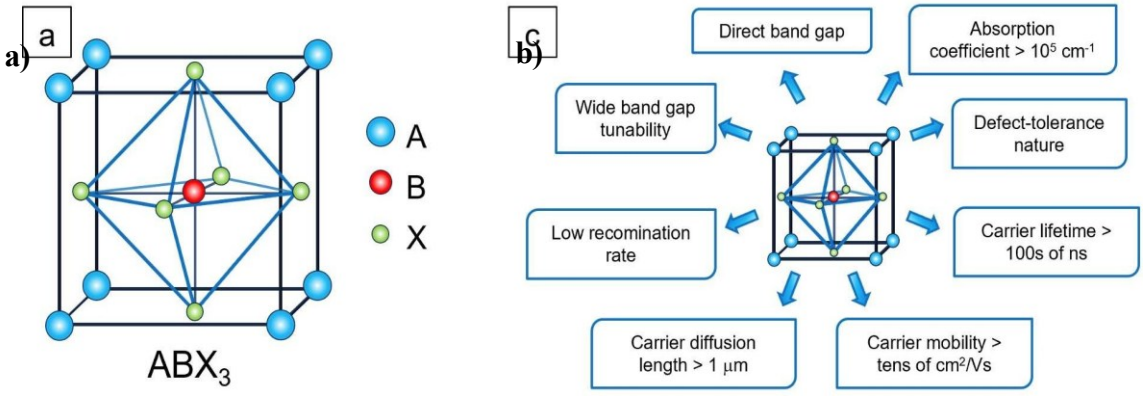

Figure 13. a) 3D-halide perovskite (HP) structure ABX_3. **b)** Main optoelectronic properties of perovskite materials.[51]

Over the past decade, perovskite solar cells (PSCs), which employ HPs as the active layer, have achieved remarkable progress, with power conversion efficiencies rising from 3.8% in 2009 to a record 27%.[22] Beyond their remarkable optoelectronic properties, perovskites offer two additional compelling advantages:

- solution-based processability at relatively low temperatures (100–150 °C), enabling cost- and energy-efficient fabrication with an energy payback time (EPBT) shorter than one year;
- compatibility with transparent, conductive, and flexible substrates, making them highly attractive for future photovoltaic markets.

The distinctive characteristics of hybrid perovskites (HPs), combined with the rapid progress achieved in the performance of perovskite solar cells (PSCs), have paved the way for their integration into a wide range of practical applications where photovoltaic technologies with tailored design features are required. Unlike conventional PV materials, HPs offer remarkable flexibility in tuning their intrinsic properties through targeted materials engineering, making them adaptable to the specific demands of different applications. Such tunability encompasses parameters such as bandgap energy, transparency, colour, mechanical flexibility, weight, size, and thermal management, thereby enabling multifunctional capabilities that include aesthetic appeal, visual comfort, and heat insulation.[47,49]

Device Structure

Perovskite solar cells (PSCs) are typically composed of a multilayer architecture. The basic device structure includes an absorber layer, an electron transport layer (ETL), a hole transport layer (HTL), a transparent conductive oxide (TCO), and metallic contact. Owing to the ambipolar semiconducting nature of hybrid perovskites, which combine strong light absorption with the ability to transport both electrons and holes, PSCs can be realized in two planar configurations: the conventional *n-i-p* structure, where the perovskite is deposited on an ETL

(**Figure 13a**), and the inverted *p-i-n* structure, where it is deposited on an HTL (**Figure 13b**). Upon light absorption, the perovskite crystal generates electron–hole pairs that are separated and driven in opposite directions by the charge-selective transport layers. The charges are then collected at the respective electrodes, i.e., the TCO and the back metal electrode (**Figure 13c**).[52,53]

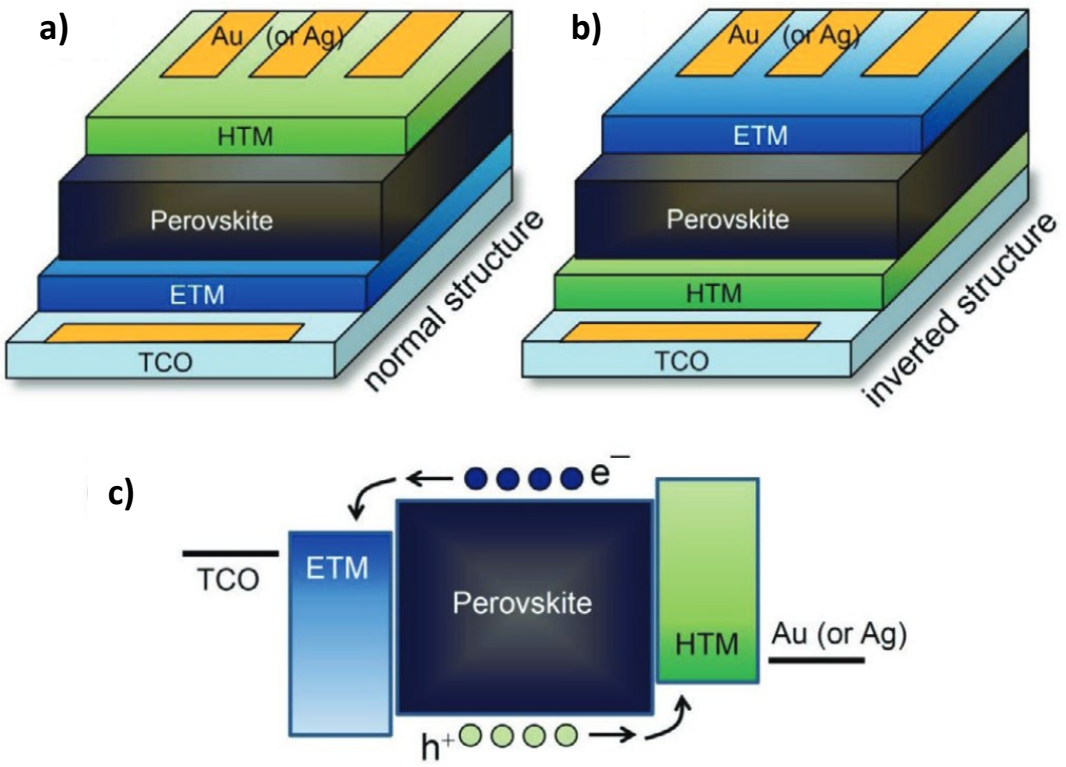

Figure 14. Perovskite solar cell architectures: **a)** regular n-i-p structure, **b)** inverted p-i-n structure. **c)** Energy level diagram showing carrier transport.[52]

1.4 Semi-transparent Photovoltaics

Semi-transparent photovoltaics (ST-PVs) are an emerging class of solar devices designed to simultaneously generate electricity while allowing partial transmission of visible light. Their operation relies on balancing light absorption for power generation with controlled transparency. Thanks to the tunable optical and electronic properties of materials such as perovskites, ST-PVs can be tailored in terms of transparency, colour neutrality, and efficiency. This makes them promising for applications such as building-integrated photovoltaics (BIPV), greenhouses, and other contexts where aesthetics, visual comfort, and energy harvesting need to be combined within the same device.

Key Optical Parameters

In addition to the standard photovoltaic figures of merit: power conversion efficiency (PCE), open-circuit voltage (Voc), short-circuit current density (Jsc), and fill factor (FF), semi-transparent solar cells (ST-SCs) require the assessment of optical properties, which are equally critical for their practical application in building-integrated photovoltaics (BIPV) and tandem architectures. Among these, two parameters stand out as key performance indicators: the Average Visible Transmittance (AVT) and the Light Utilization Efficiency (LUE).

AVT quantifies the fraction of visible light transmitted through the solar cell, weighted by both the human eye's spectral response and the standard solar spectrum. It provides an objective metric of the cell's transparency, tipically in the 380–780 nm range, which directly impacts both aesthetics and functionality when devices are integrated into windows or façades. The AVT is defined by integrating the optical transmittance spectrum of the device with respect to both the photopic response of the human eye and the solar irradiance spectrum. Experimentally the AVT of a semi-transparent solar cell is derived from its optical transmittance spectrum, acquired using a UV-Vis-NIR spectrophotometer. The raw transmittance spectrum is processed numerically to compute the AVT according to the definition:

$$\mathrm{AVT} = \frac{\int \mathrm{T}(\lambda)\mathrm{P}(\lambda)\mathrm{S}(\lambda)\mathrm{d}(\lambda)}{\int \mathrm{P}(\lambda)\mathrm{S}(\lambda)\mathrm{d}(\lambda)} \quad (7)$$

where: $T(\lambda)$ is the transmittance of the device at wavelength λ, $P(\lambda)$ is the photopic response function of the human eye, and $S(\lambda)$ is the solar spectral irradiance (AM1.5G reference). AVT is conventionally measured at normal incidence (0°). For practical applications, angular dependence may also be evaluated. Transparency and efficiency are generally in competition. To capture this duality, the Light Utilization Efficiency (LUE) was introduced as a comprehensive figure of merit. LUE combines the optical and electrical performance parameters into a single value that allows direct comparison of different semi-transparent technologies:

$$\mathrm{LUE} = \mathrm{AVT} \cdot \mathrm{PCE} \quad (8)$$

High LUE values indicate a well-optimized balance between aesthetics (sufficient transparency) and function (sufficient electricity generation), while low LUE values indicate that either transparency or efficiency is being compromised excessively.[54,55]

Current Semi-transparent Technology

According to their light-transmission mechanism, transparent photovoltaic (TPV) technologies are generally divided into two categories: spatially selective light-transmission photovoltaics and transparent thin-film photovoltaics.

As schematically presented in **Figure 14**, the spatially selective strategy involves the segmentation of opaque photovoltaic units, such that visible light passes through the uncoated regions between adjacent cells. This approach is applicable to various opaque photovoltaic devices, including Si, CIGS, CdTe, and perovskite solar cells. Although this strategy ensures partial transparency, it generally results in compromised visual appeal. The introduction of microporous structures provides a promising route toward improved transparency, though it simultaneously increases manufacturing complexity and costs.

Transparent thin-film photovoltaic technologies are characterized by devices capable of transmitting visible light through their structure. To achieve this functionality, each layer, including the photoactive layer, charge transport layers, and electrodes, must exhibit a high transparency. The transparency of these devices can be enhanced either by reducing the thickness of the photoactive layer or by employing wavelength-selective photoactive materials. Among these strategies, thickness reduction represents the simplest approach. According to the Beer–Lambert law, reducing the absorber thickness increases visible light transmission. This non-wavelength-selective method is broadly applicable to a wide range of thin-film photovoltaic systems, including CIGS, CdTe, perovskite, and organic solar cells. In contrast, the use of wavelength-selective photoactive materials enables STPVs to transmit visible light while harvesting energy from the ultraviolet (UV) and/or near-infrared (NIR) regions. This approach is considered wavelength-selective and is predominantly implemented in organic material-based devices. The spectral selectivity originates from electronic transitions between ground and excited states, which are dictated by the molecular structure of the organic compounds. Perovskite materials demonstrate remarkable compatibility with all presented approaches for achieving semi-transparency. This exceptional versatility across all transparency methodologies, combined with their outstanding optoelectronic properties and low-cost processing, positions perovskites as the most promising material platform for semi-transparent photovoltaic applications.[54–60]

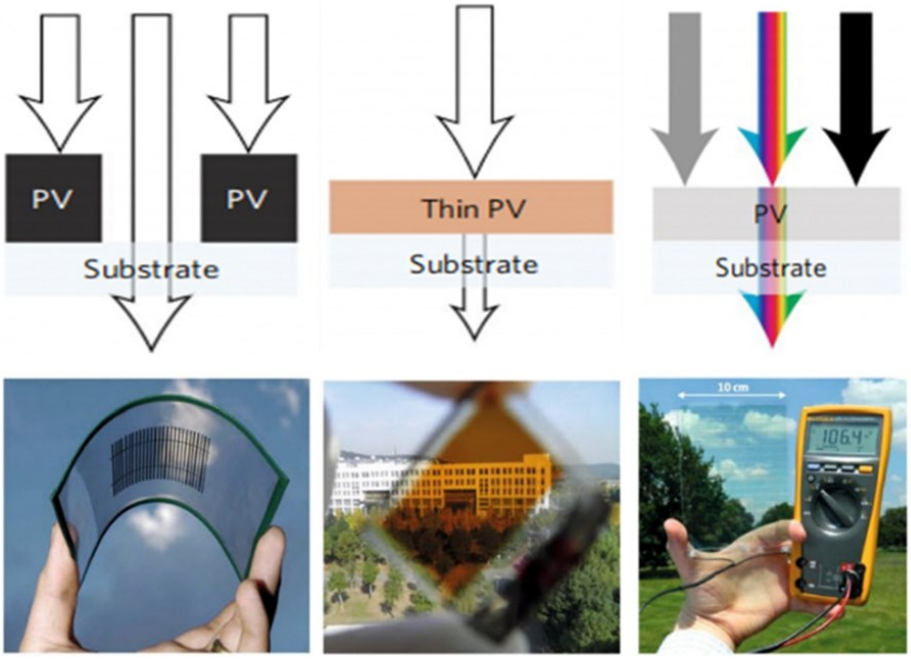

Figure 15. Illustration of three TPV approaches: (**left**) spatially selective light transmission; (**center**) transparent thin-films with reduced photoactive layer thickness; (**right**) transparent thin-films using wavelength-selective photoactive materials.[55]

Perovskite Semi-transparent Solar Cells

In recent years, perovskite solar cells (PSCs) have become a major research hotspot within semi-transparent photovoltaics. Strategies to control the transparency of the perovskite absorber layer include controlled patterning, porosity modulation, thickness engineering, and bandgap tuning (**Figure 15a**).

Semi-transparency in perovskite solar cells can be achieved through patterning techniques, where the perovskite layer is deposited in a spatially selective manner rather than as a uniform film. In this approach, "thicker" and opaque perovskite regions are laterally separated by transparent areas, enabling light transmission while preserving efficient photon absorption in the active regions.[61–63]

Porosity tuning in perovskite films is typically achieved by reducing surface coverage through hydrophobic substrate treatments. This approach allows controlled modification of film morphology, enhancing transparency while maintaining photovoltaic performance.[64,65]

Thickness control can be achieved by adjusting the molar concentration of the precursor solution, with thin absorbers often fabricated through spin-coating of

low-concentration solutions to enhance light transmittance. Alternatively, fine control can also be accomplished by modifying deposition parameters and annealing protocols, thereby avoiding direct changes in precursor concentration. Importantly, the ability to reduce the thickness of the perovskite layer without compromising photovoltaic performance stems from its inherently high optical absorption coefficient, which enables efficient photon harvesting even with reduced film thickness. As a result, ST-PSCs can achieve a favorable balance between average visible transmittance (AVT) and power conversion efficiency (PCE).[66–70]

Without changing the absorber thickness, transparency can also be achieved by using a wider band gap perovskite with a higher average visible light transmittance. The bandgap of halide perovskites can be effectively tuned by substituting the X-site halide anion (**Figure 15b**). For example, $CsPbBr_xI_{3-x}$, $MAPbBr_xI_{3-x}$, and $FAPbBr_xI_{3-x}$ exhibit bandgaps ranging from approximately 1.73 to 2.38 eV, 1.59 to 2.30 eV, and 1.48 to 2.30 eV, respectively.[71,72] This compositional tuning is accompanied by a gradual change in the film color from reddish-brown to yellow with increasing bromide content. **Figure 15c** presents a schematic of the energy levels of these representative perovskites, highlighting the versatility in bandgap modulation. A miscibility limit exists for Br contents exceeding ~40%, beyond which bromide-rich mixed halide perovskites undergo severe photo-instability and phase separation due to ionic exchange and/or migration under illumination. To mitigate this issue in Br/I mixed compositions, partial substitution of FA with Cs has proven to be an effective strategy, yielding phase-stable hybrid perovskites that enable the fabrication of stable semi-transparent perovskite solar cells (ST-PSCs). Furthermore, when Cs fully occupies the A-site, the resulting inorganic perovskite exhibits excellent thermal and photostability, making it a highly promising photoactive layer for ST-PSCs.[73,74]

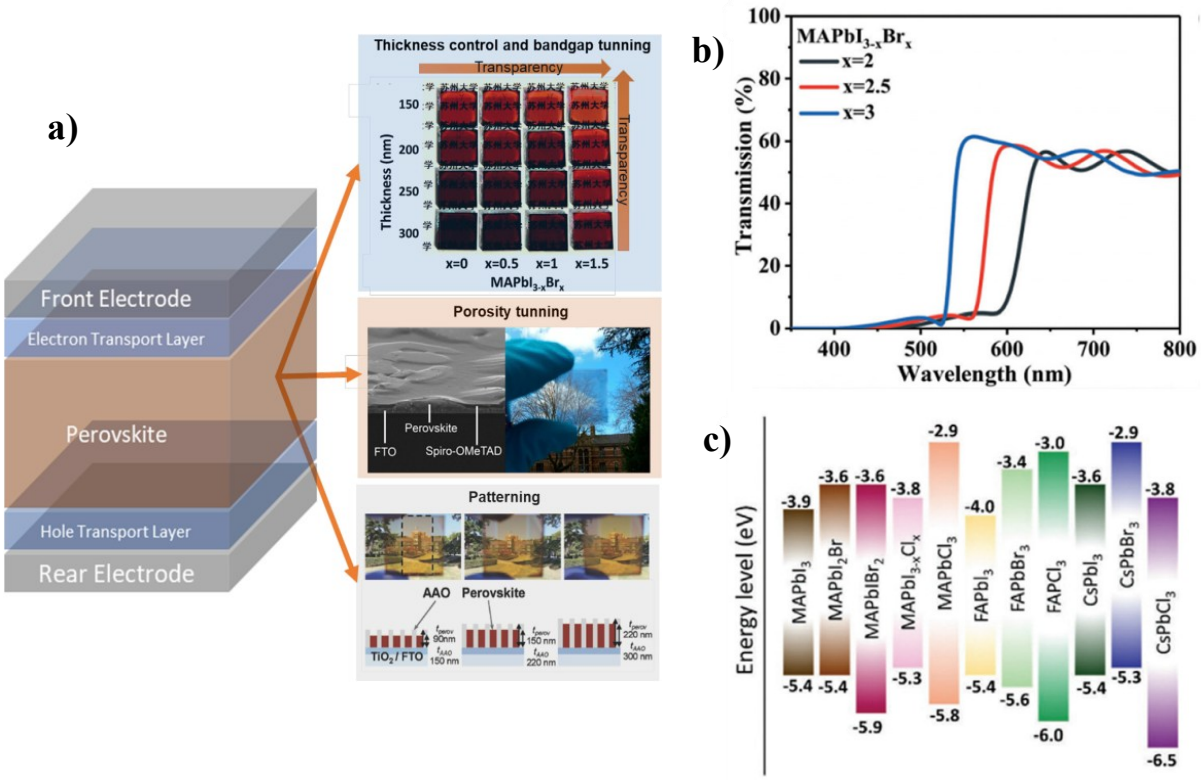

Figure 16. a) Strategies for fabricating semi-transparent perovskite solar cells.[101] **b)**Transmittance spectra of perovskites with different amount of bromide.[55] **c)** Schematic energy levels of typical perovskite materials with varied bandgaps.[102]

Over the years, low-dimensional halide perovskites (LD-HPs) have emerged as a promising strategy to overcome the stability limitations of their 3D counterparts. Although they generally exhibit lower optoelectronic performance, LD-HPs provide superior environmental and photostability. These materials are derived from conventional 3D perovskites through the intercalation of bulky organic cations (R),typically alkyl chains or aromatic groups with amine functionality, between the inorganic BX_6 octahedral slabs. Because such large cations cannot fit into the octahedral framework, they separate the inorganic layers, leadingto the formation of two-dimensional (2D) perovskite sheets.[75,76]

The most common LD-HPs are Ruddlesden-Popper (RP) perovskites, in which R is a monoamine cation, while the use of diamine cations gives rise to Dion-Jacobson (DJ) phases. The number of inorganic layers between organic spacers is denoted by n (**Figure 17**). For n = 1, a pure 2D perovskite is obtained, whereas in the limit $n \to \infty$ the structure approaches a 3D perovskite. Typically, quasi-2D

perovskites correspond to n values between 2 and 5-6, while for higher n values the material behaves almost like its 3D analogue. Importantly, as the number of inorganic layers increases, both the bandgap and the exciton binding energy decrease, making quasi-2D perovskites a suitable alternative to wide-bandgap 3D counterparts for semi-transparent photovoltaic applications.[77]

Nevertheless, charge transport across the insulating organic spacer layers in LD-HPs is strongly hindered, resulting in inefficient carrier extraction at the contacts. To address this challenge, extensive efforts have been directed toward controlling the vertical alignment of the inorganic perovskite slabs within thin films, thereby enhancing charge transport pathways and device performance.[78]

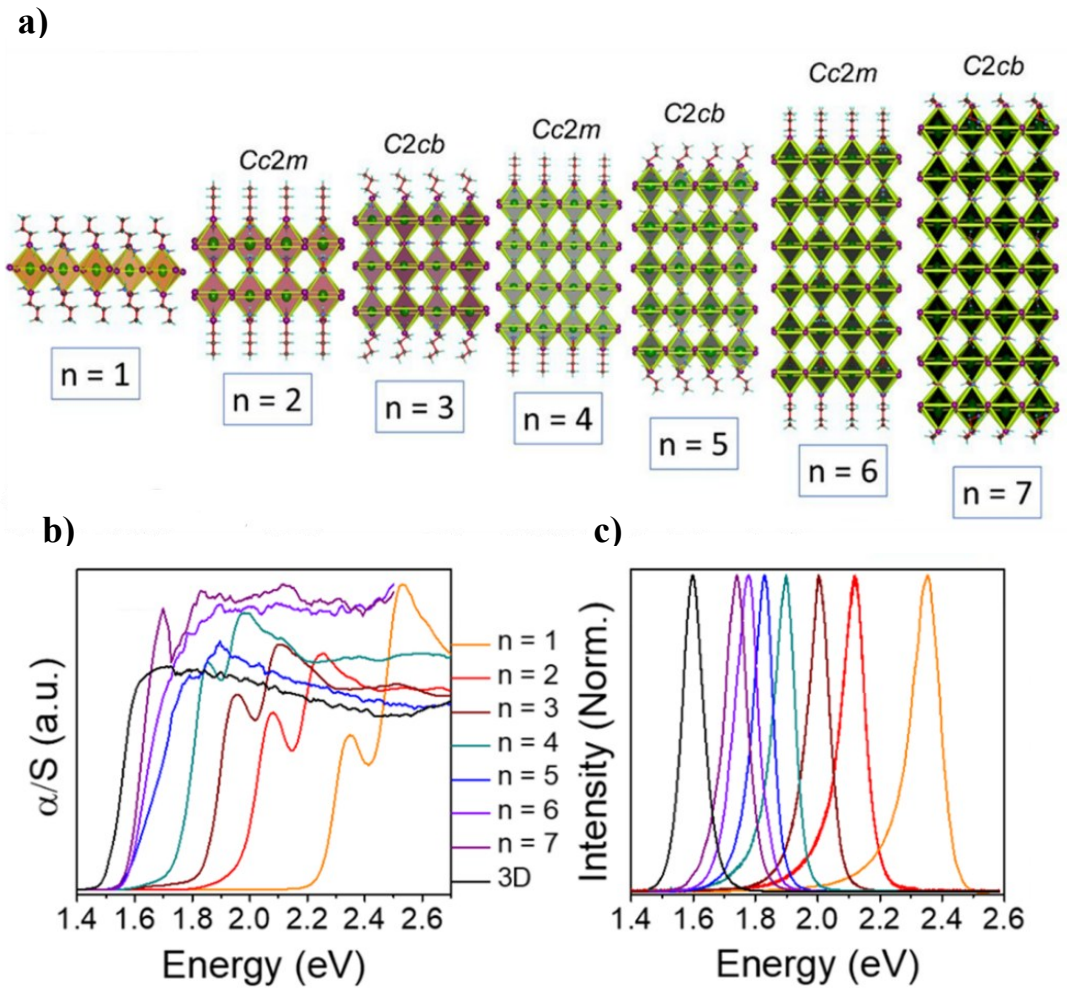

Figure 17. a) Crystal structure, **b)** absorption spectra and c) PL spectra of quasi-2D perovskites with different *n* values.[77]

Chapter 2
Materials and Methods

This section describes the materials, experimental procedures, and characterization techniques used in the fabrication and analysis of perovskite solar cells. A *p-i-n* device architecture was selected, and the choice of chemicals, solvents, substrates, and transport layers is outlined.

Indium tin oxide (ITO), composed of indium oxide (In_2O_3) with 3–10 wt% tin oxide (SnO_2), was employed as the transparent conductive oxide (TCO) owing to its excellent electrical conductivity, high optical transmittance, environmental stability, and favorable surface morphology.[79,80] As the hole transport layer (HTL), the self-assembled monolayer [2-(3,6-dimethoxy-9H-carbazol-9-yl)ethyl]-phosphonic acid (MeO-2PACz) was chosen due to its efficiency as a hole-selective contact, facilitated by phosphonic acid anchoring groups that strongly bind to the ITO surface.[81] For the electron transport layer (ETL), [6,6]-phenyl-C_{61}-butyric acid methyl ester (PCBM) was utilized because of its advantageous properties, including high electron mobility and compatibility with low-temperature processing. Silver (Ag) was adopted as the metal electrode. Because silver has a relatively high work function compared to the LUMO of PCBM, a significant barrier arises at the PCBM/Ag interface, which leads to electron accumulation and interfacial recombination, thereby reducing device performance. The insertion of a thin BCP layer effectively mitigates this issue by aligning the energy levels, facilitating efficient electron extraction, and simultaneously acting as a hole-blocking layer.[82]

The deposition methods for each layer, with particular focus on the perovskite absorber, are presented in detail. Furthermore, the optical, morphological, and photovoltaic characterization techniques employed to evaluate device performance are described.

2.1 Chemicals

Chlorobenzene (CB, extra dry, 99.8%), dimethyl sulfoxide (DMSO, Extra Dry, ≥99.8%) and N,N-dimethylformamide (DMF, Extra Dry, 99.8%) chloroform (CF, extra dry 99.8%) were purchased from Acros Organics. 2-Propanol (IPA, ≥99.8%) and Lead Iodide (PbI_2, >99.99%) were purchased from TCI.

Formamidinium iodide (FAI, >99.99 %), methylammonium chloride and 4-fluoro-phenylethylammonium iodide (F-PEAI, >99%) were purchased from GreatCell Solar Materials. PCBM was purchased from Lumatec. Ethanol (Extra Dry, 99.8 %) and bathocuproine (BCP) were purchased from Sigma Aldrich. All solutions were prepared in an Argon-filled glovebox, while the deposition of each layer of the solar cell was performed in a Nitrogen-filled glovebox.

2.2 Spin Coating

Spin coating is a laboratory technique for rapidly producing thin films and coatings by applying liquid-based solutions onto a rotating substrate. The process consists of several stages: first, the coating solution is deposited onto the substrate surface, with the amount depending on the liquid viscosity and substrate size. During the acceleration stage, the substrate accelerates to a predetermined spinning speed, causing the centrifugal force to spread the solution across the surface. The target spinning speed is specifically chosen based on the desired film thickness. The liquid flows radially outward while excess material is expelled from the perimeter as droplets. As the substrate continues spinning at higher speeds, rapid solvent evaporation becomes the primary thinning mechanism, ultimately producing a uniform coating layer. The final membrane thickness is controlled by critical parameters including solvent evaporation rate, substrate spinning velocity (spin rate), solution viscosity, precursor volume, rotational time, and solution or solid concentration. These experimental parameters are essential for controlling membrane formation and achieving the desired coating characteristics. The relationship between these parameters and the final film thickness can be mathematically described using the Meyerhofer model, which considers the balance between centrifugal forces and solvent evaporation during the spin coating process. The final thickness of the film can be determined by the following equation:

$$H_f = C_0 H_0 = C_0 \left(\frac{3\mu C_0 E}{2(1 - C_0)\rho\omega^2} \right)^{1/3} \tag{9}$$

where H_f is the final film thickness, C_0 is the initial solute concentration, E is the solvent evaporation rate, ω is the angular spinning speed, and μ and ρ are the solution viscosity and density, respectively. The term H_0 represents the film thickness at the transition between flow-dominated and evaporation-dominated thinning regimes.[83,84]

2.3 Device Fabrication

Pre-patterned ITO/glass substrates underwent sequential ultrasonic cleaning in acetone and 2-propanol (IPA), with 15-minute treatments in each solvent. Substrates were dried with N_2 airflow and oxygen plasma treated using a ZEPTO plasma cleaner (Diener Electronic) at 100 mW for 10 minutes. All substrates were subsequently transferred to a glovebox for layer deposition. MeO-2PACz was dissolved in ethanol at a concentration of 1 mM, and 40 μL of solution was spin-coated onto the ITO/glass substrates at 3000 rpm for 30 seconds (acceleration: 1500 rpm/s), followed by thermal annealing at 100°C for 10 minutes. A 0.6 M perovskite precursor solution was prepared by dissolving PbI_2 and FAI powders in DMF/DMSO (4:1 v/v) with 5% excess PbI_2. For bulk treatment, MACl (35 mol%) was added to the solution. This stock solution was then diluted with DMF/DMSO (4:1 v/v) to achieve a final concentration of 0.5 M. The perovskite layer was deposited by spin-coating 30 μL of solution onto the MeO-2PACz layer using a three-step program: first at 1000 rpm for 12 s, followed by 5000 rpm for 27 s, and concluding with a 4 s deceleration phase. During the second step, 150 μL of chlorobenzene (CB) was dispensed onto the spinning substrate 9 s after the step began to initiate antisolvent quenching. The resulting films were annealed at 100°C for 30 minutes. For the surface passivation of the perovskite layer, 50 μL of a 0.005 M F-PEAI solution in a chlorobenzene:isopropanol (9:1) solvent mixture was dynamically spin-coated at 5000 rpm for 30 s. Following this step, the electron transport layer (ETL) was deposited by spin-coating 20 μL of a 15 $mg \cdot mL^{-1}$ PCBM solution in chloroform onto the perovskite film. Subsequently, 40 μL of a 1 $mg \cdot mL^{-1}$ bathocuproine solution in isopropanol was deposited onto the PCBM layer. Finally, a silver

layer with a thickness of 80 nm was thermally evaporated to define the top electrode. The deposition was carried out at a rate of 0.01 $nm \cdot s^{-1}$ for the initial 5 nm, followed by 0.02 $nm \cdot s^{-1}$ from 5 to 15 nm, and 0.08 $nm \cdot s^{-1}$ for the remaining thickness. The resulting devices exhibited pixels with an active area of 0.045 cm^2.

2.4 Material Characterization

UV−Vis Spectroscopy

UV-Vis transmittance spectra were recorded on a Perkin Elmer Lambda 1050+ UV-vis spectrophotometer. Scan range was set between 250 nm and 850 nm for all measurements. The UV-Vis spectra were acquired for device stacks with the configuration Glass/ITO/MeO-2PACz/$FAPbI_3$/PCBM/BCP. The silver electrodes were excluded from the measurements, as they are opaque in the fabricated devices.

Field Emission Scanning Electron Microscopy

Morphological characterization is recorded using a Field Emission Scanning Electron Microscope (FESEM, JEOL JSM-7600F, 5 kV, and 10 mA). FESEM was employed both to determine the thickness of the perovskite layer and to acquire top-view images for the evaluation of film morphology. A slight thickness variation (~10–15 nm) in the perovskite cross-section was observed when comparing fast and slow scanning modes, most likely arising from sample charging effects, even though grounding and platinum sputtering were employed to mitigate this issue. Nevertheless, slow scanning was selected, as it was the only approach that yielded clear and reliable images.

Photoluminescence – Time Resolved Photoluminescence Spectroscopy

The PL and TRPL measurements employ a dual-mode laser source (PicoQuant, LDH series D-C-470) operating at 470 nm, capable of both continuous wave (CW) and pulsed excitation with adjustable repetition rates ranging from single shot to 40 MHz. The excitation beam is directed onto the sample using a 500 nm long-pass dichroic mirror and focused through lens L1. Sample positioning is achieved through a precision z-axis micrometric stage to ensure optimal

alignment and focusing. The photoluminescence signal was collected in epi-fluorescence configuration through the same objective lens (L1) and transmitted through the dichroic mirror. To eliminate stray light contamination, an additional long-pass filter was positioned before lens L2, which focused the collected signal into an optical fiber coupled to the interferometer. The interferometer output was connected via optical fiber to a single photon detector (SPD). A time tagger acquires signals from both the SPD and the laser synchronization output, facilitating time-correlated single photon counting (TCSPC) measurements. USB connections interface the interferometer and time tagger with a computer system for software-based analysis and data acquisition.

All measurements were conducted at room temperature and in ambient air conditions. The excitation pulses were provided by a PicoQuant diode laser with 470 nm wavelength, 40 MHz repetition rate and average power of 20-30 μW measured by a Si power-meter; the spot-size is approximately 40 μm. PL/TRPL measurements were conducted exciting and collecting from glass side on full devices.[86]

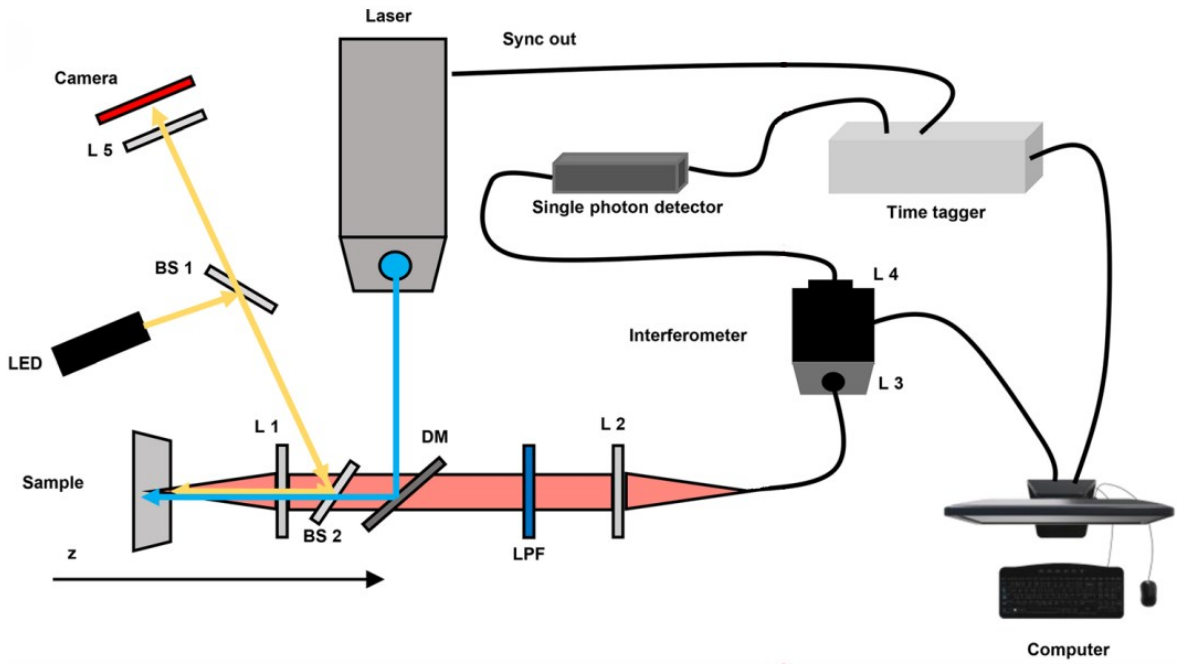

Figure 18. Experimental PL and TRPL set-up.[86]

2.5 Device Characterization

Current-Voltage Measurements

Current density-voltage measurements were performed in ambient conditions under simulated AM 1.5G light with an intensity of 100 $mW \cdot cm^{-2}$ (Wavelabs-Sinus 70). The intensity was calibrated using a Si reference cell. Cells were scanned using a Keithley 2450 source-meter backward and forward from 1.2 V to − 0.1 V, with a scanning velocity of 100 $mV \cdot s^{-1}$. The pixel area was 3 mm by 1.5 mm measured with a shadow mask.

External Quantum Efficiency

External quantum efficiency (EQE) represents the ratio of collected charge carriers to incident photons at each wavelength. This wavelength-dependent parameter is determined by illuminating the solar cell with monochromatic light at various wavelengths and measuring the resulting photocurrent output. The EQE spectrum reveals the device's spectral response and is defined as:

$$EQE(\lambda) = \frac{I_{ph}(\lambda)}{q\Psi_{ph,\lambda}} \tag{10}$$

where q is the elementary charge and $\Psi_{ph}(\lambda)$ is the incident spectral photon flux at wavelength λ. Since direct measurement of photon flux is not feasible, an indirect approach is employed using a calibrated reference device. A photodetector or solar cell with precisely known EQE characteristics serves as the reference standard. This calibration measurement yields:

$$\Psi_{ph,\lambda} = \frac{I_{ph}^{ref}(\lambda)}{qEQE_{ref}(\lambda)} \tag{11}$$

combining Equations 10 and 11 we therefore obtain

$$EQE(\lambda) = EQE_{ref}(\lambda)\frac{I_{ph}(\lambda)}{I_{ph}^{ref}(\lambda)} \tag{11}$$

Experimentally, external quantum efficiency measurements were performed under ambient conditions using a Cicci Research Arkeo steady-state test module**.** **Figure 18** shows a schematic representation of the experimental setup. The incident light was first directed through a monochromator for wavelength selection, then passed through an optical chopper before reaching the sample. The solar cell was connected to a voltage source to measure the extracted charge carriers. A calibrated photodiode was used to quantify the incident photon flux, enabling the calculation of incident photon-to-current efficiency (IPCE) spectra as a function of wavelength. Measurements were conducted across a wavelength range of 300-900 nm.[10,87]

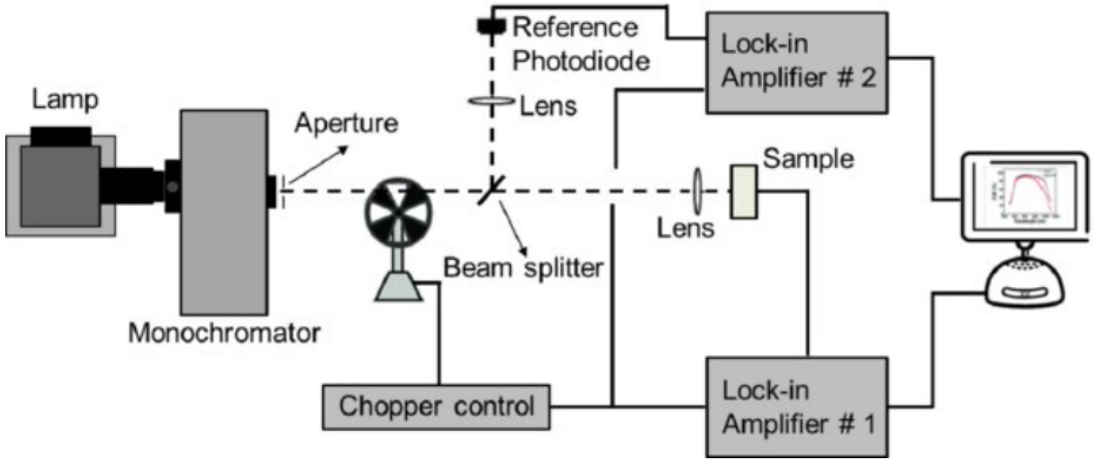

Figure 19. EQE experimental measurement set-up.[87]

Transient Photovoltage and Photocurrent

Transient photovoltage (TPV) and transient photocurrent (TPC) techniques investigate the temporal evolution of photogenerated charges in solar cells. TPV measures the voltage decay at open-circuit following a light pulse, directly probing carrier recombination dynamics and effective lifetimes. Conversely, TPC monitors the current response under short-circuit conditions, revealing charge extraction rates and transport limitations. TPV and TPC analyses were performed in ambient air conditions with a Cicci Research Arkeo transient tests module. Measurements were conducted under constant 1 sun illumination and the constant bias was perturbed with short light pulses of 200 µs.

Stability Tests

Device stability was evaluated through two complementary protocols: shelf-life stability and operational maximum power point (MPP) tracking. For shelf-life assessment, unencapsulated devices were stored in the dark within a nitrogen-filled glovebox and periodically tested to monitor passive degradation over time. Operational stability was investigated using continuous MPP tracking under N_2 atmosphere in a Litos Lite stability box (Fluxim), with samples subjected to constant illumination from a Wavelabs solar simulator. The illumination spectrum employed for stability measurements matched that used for current density-voltage characterization, ensuring consistent testing conditions

Chapter 3
Results and Discussion

3.1 Transparency Study

In this work, we introduce an alternative strategy to wide-bandgap perovskites based on formamidinium lead iodide ($FAPbI_3$), a narrow-bandgap material typically employed in opaque architectures. By precisely engineering the $FAPbI_3$ absorber layer, we demonstrate devices that simultaneously deliver high optical transparency and competitive power conversion efficiency. This approach circumvents the intrinsic limitations of bromide-rich compositions, such as phase segregation and limited stability, establishing a pathway toward high-performance semi-transparent solar cells suitable for building-integrated applications. The thickness of the perovskite layer was controlled by varying the precursor concentrations in the solution. Of the different precursor concentrations investigated, the 0.5 M and 0.6 M formulations demonstrated optimal performance, achieving average visible transmittance (AVT) values above 15% coupled with high photovoltaic efficiency, as will be discussed in detail in the following sections.

UV-Vis Spectra

To quantify the impact of thickness on light transmission, we measured the UV-Vis absorption spectra of the full device stack (Glass/ITO/MeO-2PACz/ $FAPbI_3$/PCBM/BCP) excluding the meal contact. As evident from the transmittance spectra (**Figure 19**), the perovskite film prepared from 0.5 M precursor solution exhibits higher light transmission. The AVT values, calculated using Equation 7, were 24.2% and 18.2% for the 0.5 M and 0.6 M precursor concentrations, respectively.

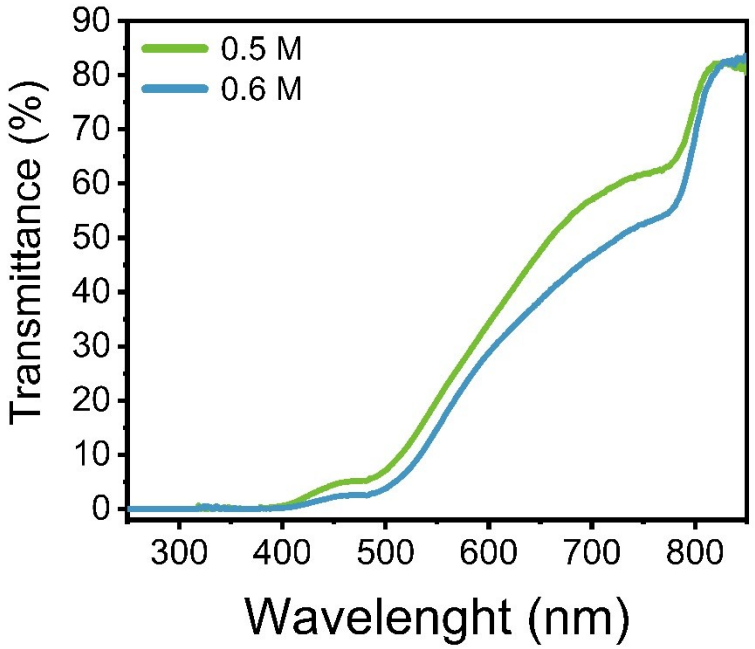

Figure 20. UV-Vis transmittance spectra of the complete device stack (Glass/ITO/MeO-2PACz/$FAPbI_3$/PCBM/BCP) for 0.5 M and 0.6 M perovskite concentrations.

Device Aesthetics

Building-integrated photovoltaics (BIPV) integrate solar cells directly into building elements such as windows and facades, serving the dual purpose of generating electricity while maintaining architectural functionality. Semi-transparent solar cells are particularly attractive for BIPV as they allow natural lighting while harvesting solar energy.

To demonstrate the compatibility of our devices with BIPV applications, we conducted visual assessment tests simulating both indoor and outdoor scenarios. **Figure 20** shows the aesthetic appearance of our semi-transparent perovskite solar cells with AVT values of 24.2% (140 nm device) and 18.2% (160 nm device). The upper panels (**a, b**) present indoor photographs under artificial lighting, while the lower panels (**c, d**) show outdoor images under natural sunlight, simulating real window applications.

Clear visibility through both devices is evident, with background features remaining easily distinguishable. Even the 160 nm device with 18.2% AVT provides sufficient transparency for practical applications, demonstrating that an

AVT of approximately 20% is adequate for BIPV implementation. The characteristic orange tint of $FAPbI_3$ could even serve as an architectural design element, adding aesthetic value beyond the functional benefits.

Figure 21. a,c) Photographs of the 140 nm device (Glass/ITO/MeO-2PACz/Perovskite/PCBM/ BCP). **b,d)** Photographs of the 160 nm device.

FESEM Measurements

Half-cell structures (Glass/ITO/MeO-2PACz/Perovskite) were characterized by Field Emission Scanning Electron Microscopy (FESEM) to determine perovskite layer thicknesses (**Figure 21 a,b**). The measurements yielded thickness ranges of 130-150 nm for 0.5 M and 150-170 nm for 0.6 M precursor concentrations, considerably thinner than the ~500 nm typically employed in opaque perovskite solar cells. Comparison of scanning modes revealed thickness variations of approximately 10-15 nm between fast and slow acquisition, attributed to residual charging effects despite implementation of grounding and platinum sputtering protocols. Given the superior image clarity obtained, slow scanning mode was selected for all measurements. From this point onward, we will refer to the devices by their thickness: 140 nm and 160 nm.

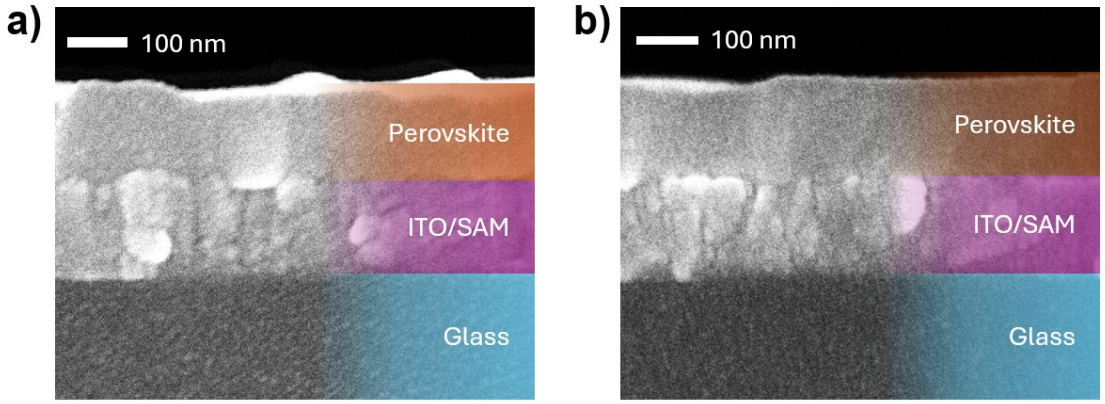

Figure 22. SEM cross section images of perovskite films with precursor concentrations of **a)** 0.5 M and **b)** 0.6 M.

3.2 Performance of Semi-transparent Solar Cells

Device performance was evaluated by measuring key photovoltaic (PV) parameters under standard AM 1.5G illumination (**Figure 22**). The champion 140 nm device achieved a short-circuit current density (J_{SC}) of 19 mA·cm^{-2}, open-circuit voltage (V_{OC}) of 998 mV, fill factor (FF) of 83.4%, resulting in a power conversion efficiency (PCE) of 15.9%. The 160 nm device delivered superior performance with J_{SC} of 20.9 mA·cm^{-2}, V_{OC} of 1031 mV, FF of 83.7%, and PCE of 18%.

As expected, the most significant difference between the two devices lies in their J_{SC} values, while V_{OC} and FF remain comparable. This current density variation of approximately 1.9 mA·cm^{-2} directly correlates with the different perovskite layer thicknesses, as the thicker 160 nm film absorbs more photons, generating additional photocurrent while maintaining similar charge extraction efficiency and recombination characteristics.

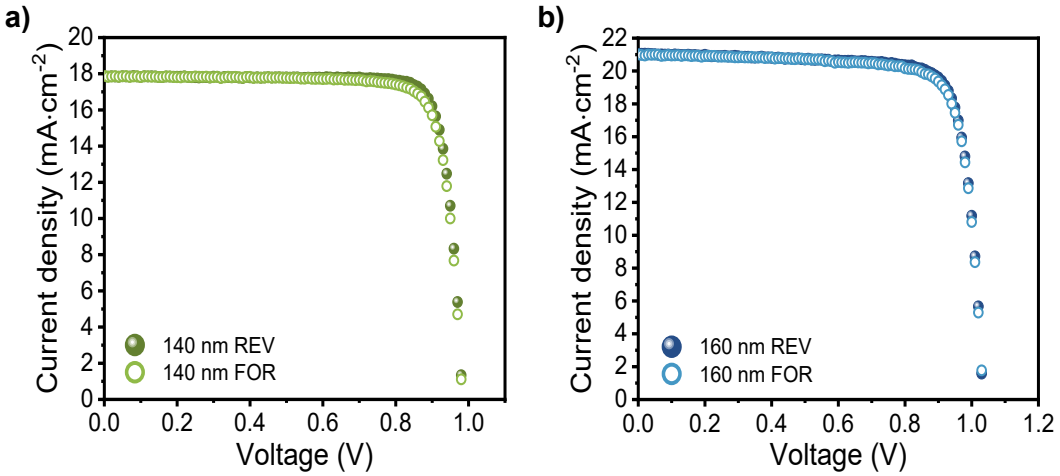

Figure 23. J–V curves under AM 1.5G illumination for the **a)** 140 nm and **b)** 160 nm devices.

		V_{OC} (mV)	J_{SC} (mA·cm^{-2})	FF (%)	PCE (%)
140 nm	Forward	998	19.1	81.0	15.4
	Reverse	998	19.0	83.4	15.9
160 nm	Forward	1023	20.8	83.4	17.7
	Reverse	1031	20.9	83.7	18.0

Table 1. Photovoltaic parameters of champion semi-transparent devices

To validate the photocurrent generation capabilities and spectral response of our semi-transparent devices, external quantum efficiency (EQE) measurements were conducted on both the 140 nm and 160 nm devices (**Figure 23**). The integrated current densities calculated from the EQE spectra showed excellent agreement with the Jsc values obtained from J-V characterization, confirming the accuracy of our electrical measurements. A detailed analysis of the EQE spectra reveals distinct differences in the light harvesting behavior between the two devices. The 140 nm device shows a significant reduction in light absorption around 650 nm compared to the 160 nm device. This wavelength-dependent variation is particularly significant as it occurs in the red portion of the visible spectrum where $FAPbI_3$ typically shows strong absorption. The reduced photon-to-electron conversion efficiency at longer wavelengths in the thinner device directly correlates with both its enhanced transparency and lower J_{SC}, as fewer photons are absorbed and converted to photocurrent in this spectral region.

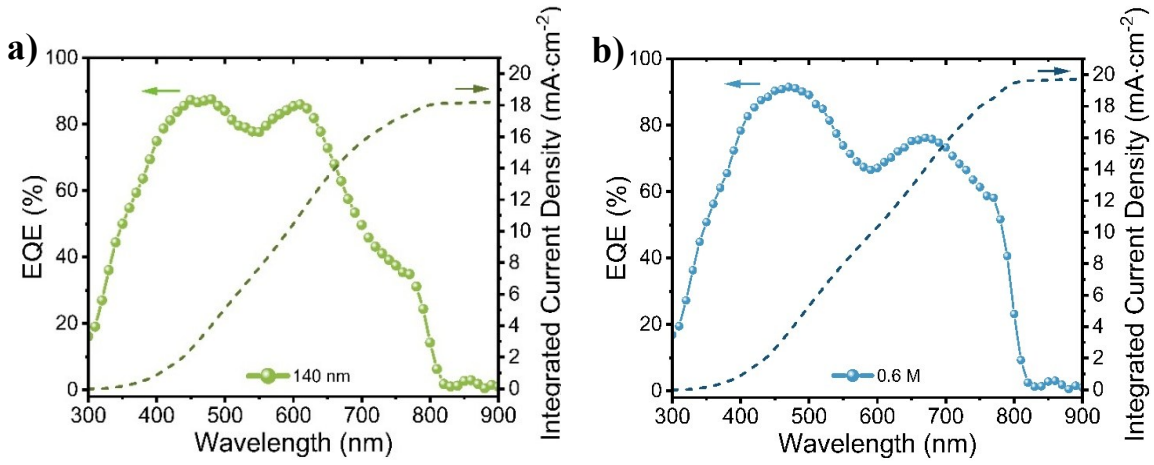

Figure 24. a) EQE of the 140 nm perovskite device. **b)** EQE of the 160 nm perovskite device.

To comprehensively evaluate the performance of our semi-transparent devices for BIPV applications, we calculated the light utilization efficiency (LUE). For the 140 nm device, with a PCE of 15.9% and AVT of 24.2%, we obtained a LUE of 3.85%. In comparison, the 160 nm device, despite its higher PCE of 18.0%, achieved a lower LUE of 3.28% due to its reduced AVT of 18.2%. A LUE value of 3% is widely recognized as a benchmark for high-performance semi-transparent solar cells, indicating an excellent balance between power generation

and optical transparency. Both our devices surpass this threshold demonstrating that our ultrathin $FAPbI_3$ approach successfully delivers superior combined optical and electrical performance, positioning our devices among the most efficient semi-transparent perovskite solar cells reported for BIPV applications.

Despite promising J_{SC} and AVT values, the devices exhibited relatively low V_{OC}, thereby limiting the overall PCE. To address this issue, surface passivation techniques were employed. Among all the passivating agents evaluated, FPEAI 5 mM in CB/IPA 9:1 yielded the most promising results.

Hereafter, the passivated devices will be referred to as 140 nm FPEAI and 160 nm FPEAI.[88,89]

3.3 Passivated Devices

UV-Vis Spectra

The initial investigation examined whether the formation of a 2D/3D heterostructure through surface passivation would negatively affect the average visible transmittance. Analysis of the transmittance spectra presented in Figure 2a demonstrates that no significant optical changes occur upon FPEAI treatment (**Figure 24**). The passivated devices exhibit AVT values of 24.85% and 18.15% for the 140 nm and 160 nm configurations, respectively. These results indicate that the surface passivation process does not compromise the transparency requirements for semi-transparent photovoltaic applications.

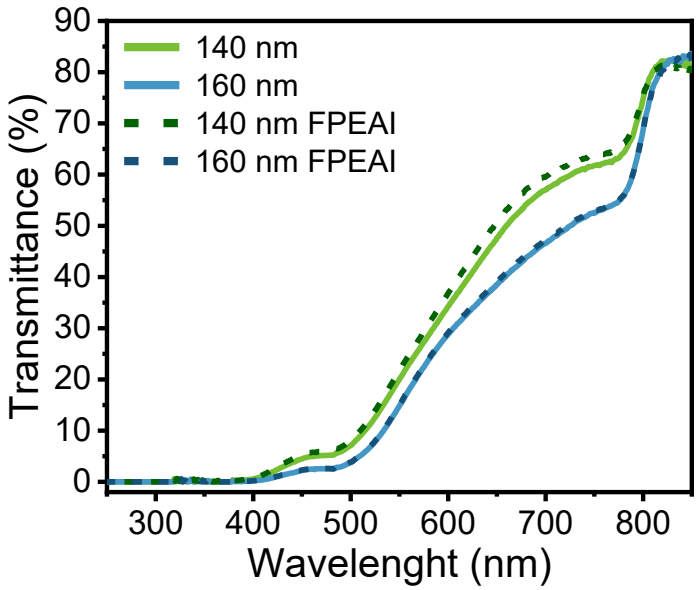

Figure 25. UV−Vis Transmittance spectra for passivated and non-passivated devices, excluding the metal contact.

Performance Evaluation

Comparative analysis of photovoltaic performance between passivated and pristine devices is presented in **Figures 25**. The FPEAI-passivated 140 nm device demonstrated enhanced parameters with V_{OC} of 1144 mV, J_{SC} of 18.2 mA·cm^{-2}, FF of 81.9%, resulting in a PCE of 17.0%. Similarly, the passivated 160 nm device achieved V_{OC} of 1145 mV, J_{SC} of 20.6 mA·cm^{-2}, FF of 82.9%, and PCE of 19.5%. A substantial improvement in open-circuit voltage exceeding 100 mV was observed for both device configurations, accompanied by efficiency gains greater than 1%. These enhancements validate the efficacy of the FPEAI surface passivation strategy in improving device performance without compromising transparency.

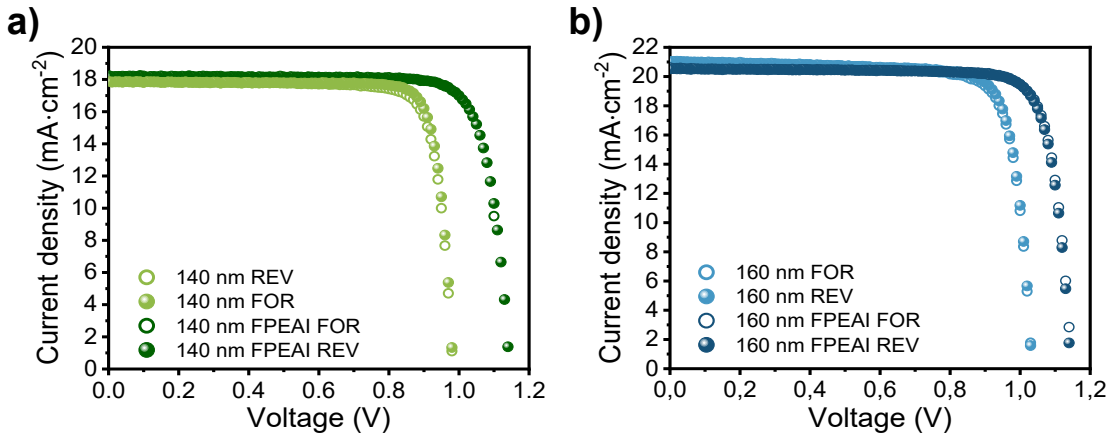

Figure 26. J−V curves of the passivated and non-passivated devices under AM 1.5G illumination.

		V_{OC} (mV)	J_{SC} (mA·cm^{-2})	FF (%)	PCE (%)
140 nm	Forward	1144	18.2	80.9	16.9
	Reverse	1145	18.2	81.9	17.0
160 nm	Forward	1148	20.6	82.2	19.5
	Reverse	1145	20.5	82.9	19.5

Table 2. Photovoltaic parameters of champion semi-transparent devices

EQE measurements were performed on both passivated and non-passivated devices to evaluate the impact of FPEAI surface treatment on the spectral response and photocurrent generation (**Figure 26**).

A particularly noteworthy observation from both figures is the negligible difference in integrated current density between passivated and non-passivated devices. This demonstrates that the FPEAI passivation layer does not compromise the current generation capability of the devices.

The EQE profiles show only minor variations between treated and untreated samples across the entire wavelength range, with both maintaining similar spectral responses. This is particularly significant as it indicates that the surface passivation strategy can be implemented without sacrificing photocurrent generation, a critical consideration for maintaining power conversion efficiency while potentially enhancing device stability.

The minimal impact on current density suggests that the FPEAI layer is

sufficiently thin or transparent to avoid parasitic absorption, while still providing the intended benefits of surface defect passivation. The effects of passivation will be further investigated through photoluminescence (PL) and time-resolved photoluminescence (TRPL) measurements to provide deeper insights into the charge carrier dynamics and recombination mechanisms.

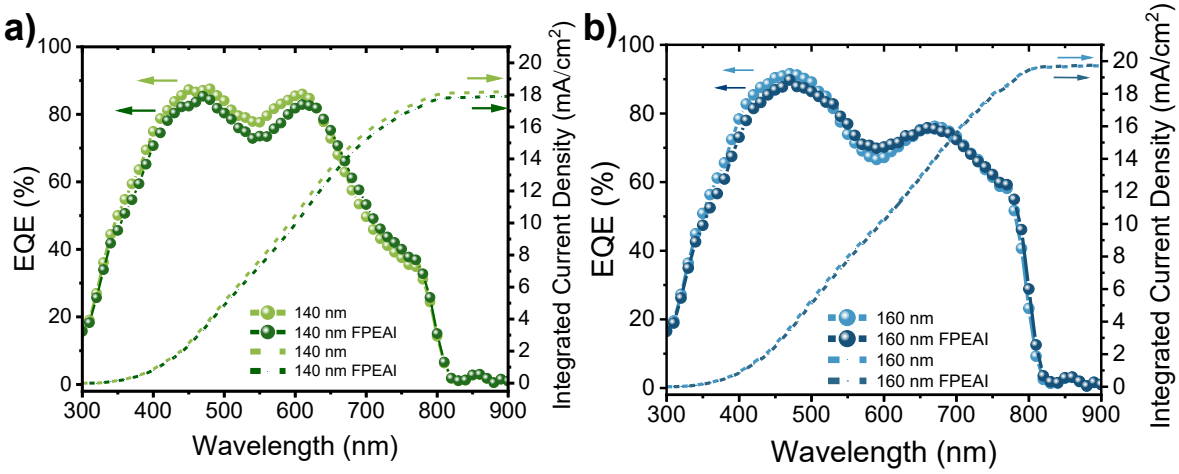

Figure 27. **a)** EQE measurement of the passivated 140 nm device, respect to the non-passivated one. **b)** EQE of the 160 nm device compared to the non-passivated counterpart.

Figure 27 presents box plots comparing the photovoltaic parameters of semi-transparent perovskite solar cells.

The open-circuit voltage (Voc) data reveals a substantial enhancement upon FPEAI treatment for both thicknesses. The 140 nm devices show an increase from approximately 980 mV to 1120 mV, while the 160 nm devices exhibit an improvement from around 1020 mV to 1150 mV. This significant Voc enhancement confirms the effective passivation of surface defects through the formation of a 2D/3D heterostructure.

The short-circuit current density (Jsc) remains relatively unchanged between pristine and passivated devices, consistent with the EQE measurements. The 140 nm devices maintain Jsc values around 18 mA/cm², while the 160 nm devices show slightly higher values near 20 mA/cm². This minimal variation in Jsc indicates that the thin 2D perovskite layer formed during FPEAI treatment does not impede charge extraction.[89,90]

The fill factor (FF) displays modest improvements with passivation, particularly

evident in the 160 nm devices where values increase from approximately 82% to 83.5%. The tighter distribution of FF values in FPEAI-treated devices, especially for the 160 nm configuration, demonstrates enhanced device reproducibility.

The power conversion efficiency (PCE) shows remarkable improvements across both thicknesses with FPEAI treatment.

Notably, the 160 nm FPEAI devices exhibit the narrowest distribution of all parameters, indicating superior reproducibility and consistent device performance, which is crucial for potential commercial applications.

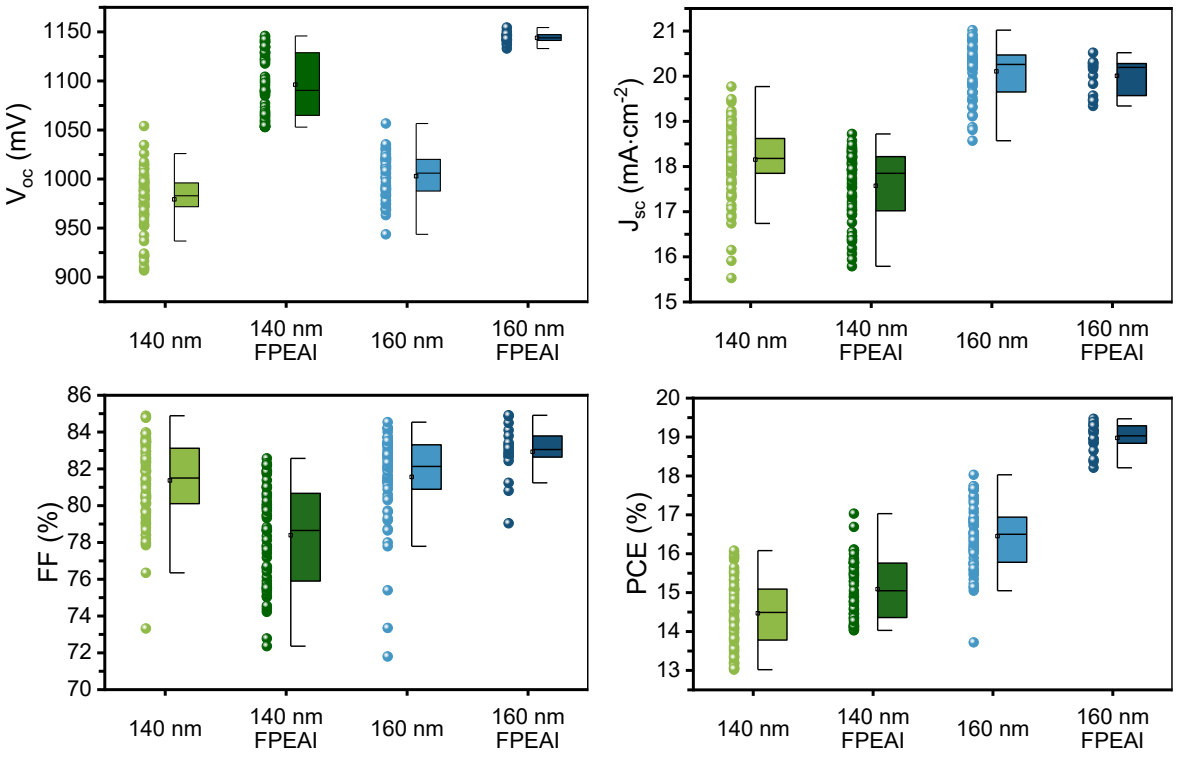

Figure 28. Box plots comparing the photovoltaic parameters (V_{oc}, J_{sc}, FF and PCE) of passivated and non-passivated devices.

Figure 28 presents a comparison between the power conversion efficiency and average visible transmittance of our highest-performing passivated devices against recently published literature data. Both devices demonstrate an exceptional balance between optical transparency (AVT) and photovoltaic performance (PCE). The 160 nm FPEAI device exceeds the performance metrics of most previously reported semi-transparent solar cells. The 140 nm FPEAI

device likewise ranks among the highest-performing systems in this category, highlighting the effectiveness of our passivation approach in achieving superior efficiency-transparency trade-offs.

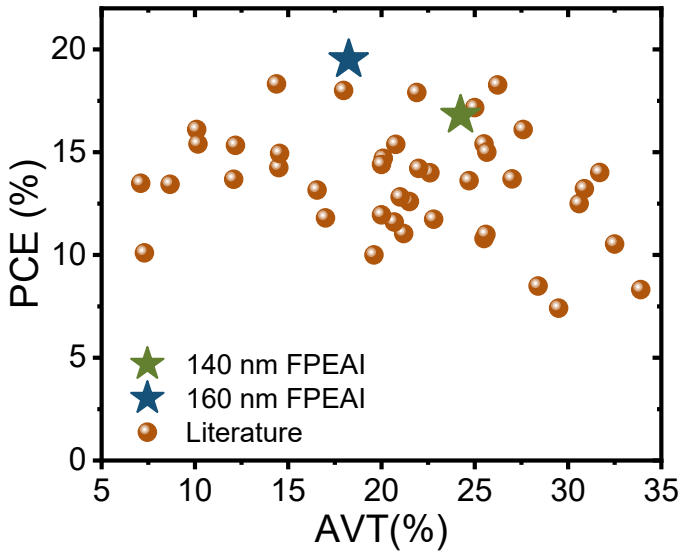

Figure 29. Power conversion efficiency (PCE) versus average visible transmittance (AVT) for our devices and literature reports.

We calculated the light utilization efficiency for the passivated devices and compared the results with their non-passivated counterparts. The passivated 140 nm device exhibited a LUE of 4.22%, which represents an improvement over the 3.85% obtained for the non-passivated device. Similarly, the 160 nm FPEAI device achieved a LUE of 3.54%, compared to 3.28% for its pristine counterpart. These results confirm that passivation enhances the light utilization efficiency in both thickness regimes,

Optical Characterization

Photoluminescence (PL) and time-resolved photoluminescence (TRPL) characterizations were performed to investigate the underlying mechanisms responsible for the improved photovoltaic performance observed in passivated devices. The passivated perovskite films exhibit substantially increased PL emission intensity relative to their pristine counterparts for both thickness

configurations (**Figure 30**). This enhanced radiative recombination indicates improved surface quality and suppressed non-radiative losses associated with surface trap states.

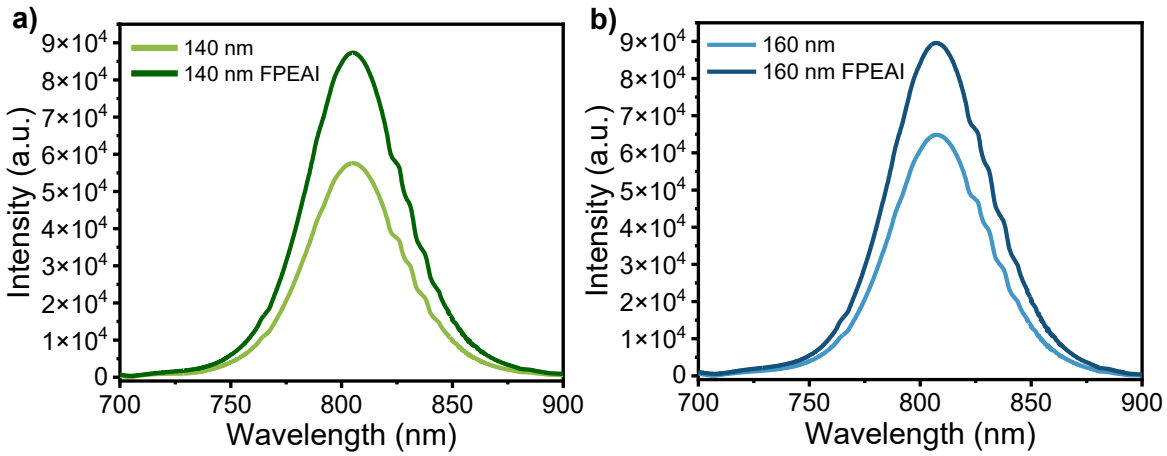

Figure 30. a,b) steady-state photoluminescence (PL) spectra of the 140 nm and 160 nm devices, before and after passivation.

Time-resolved photoluminescence (TRPL) analysis was performed to quantify carrier dynamics (**Figure 31**). TRPL curves were fitted using a mono-exponential ($y = A_1e^{-t/\tau 1}$) and a bi-exponential ($y = A_1e^{-t/\tau 1} + A_2e^{-t/\tau 2}$) fit. For the bi-exponential fit, the effective radiative lifetimes (τ_{eff}) were calculated using the following equation:

$$\tau_{eff} = \frac{A_1\tau_1^2 + A_2\tau_2^2}{A_1\tau_1 + A_2\tau_2} \quad (12)$$

The FPEAI-treated samples demonstrate extended effective radiative lifetimes (τ_{eff}) compared to their pristine counterparts, as detailed in **Table 3** and **Table 4**. Bi-exponential fitting of the TRPL decay profiles for non-passivated samples reveals two distinct lifetime components. A rapid decay component ($\tau_1 \approx 1$ ns), attributed to surface-mediated non-radiative recombination, represents the dominant recombination pathway in pristine films, accounting for 98% and 36% of the total decay amplitude in the 140 nm and 160 nm samples, respectively. Conversely, the fast component cannot be determined from the TRPL decay

curves of passivated samples (**Table S2**). This observation provides evidence for the substantial suppression of non-radiative recombination channels through surface passivation, corroborating findings reported in previous studies.[91–94]

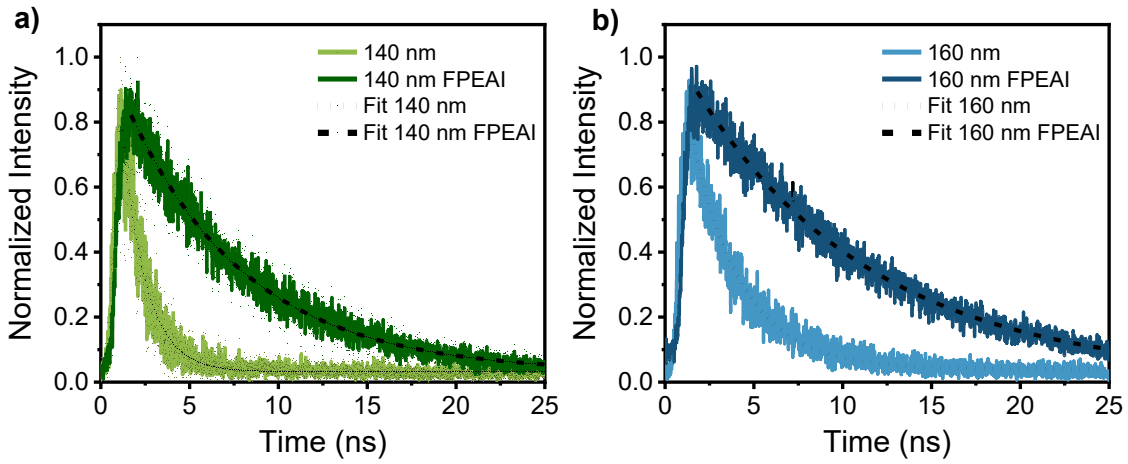

Figure 31. a.b) Time-resolved photoluminescence (TRPL) decay comparing the passivated and non-passivated devices

Samples	**A_1**	**T_{eff} (ns)**
140 nm	1.8	1
140 nm FPEAI	2.5	7
160 nm	1.9	3
160 nm FPEAI	4.0	10

Table 3. Mono-exponential fitting parameters of decay amplitude and decay time obtained from TRPL measurements

Samples	**A_1**	**τ_1 (ns)**	**A_2**	**τ_2 (ns)**	**τ_{eff} (ns)**
140 nm	2	1	0.03	10	2
140 nm FPEAI	2	6	0.7	12	9
160 nm	2	1	1	4	3
160 nm FPEAI	3	10	1	10	10

Table 4. Bi-exponential fitting parameters of decay amplitude and decay time obtained from TRPL measurements.

Optoelectronic Measurements

To investigate charge carrier dynamics under operational conditions, transient photovoltage (TPV) and transient photocurrent (TPC) analyses were performed. TPV measurements show considerably longer charge carrier lifetimes following FPEAI passivation (**Figure 32**). For the 140 nm devices, the recombination time increases from 1.13 µs to 3.51 µs, while the 160 nm devices exhibit an enhancement from 2.02 µs to 3.76 µs. This significant extension of carrier lifetimes reflects the effective suppression of recombination processes, particularly those mediated by surface defects. The improved recombination dynamics correlate well with the enhanced V_{OC} values recorded for passivated devices, confirming the beneficial impact of the FPEAI treatment on device performance.[93–97]

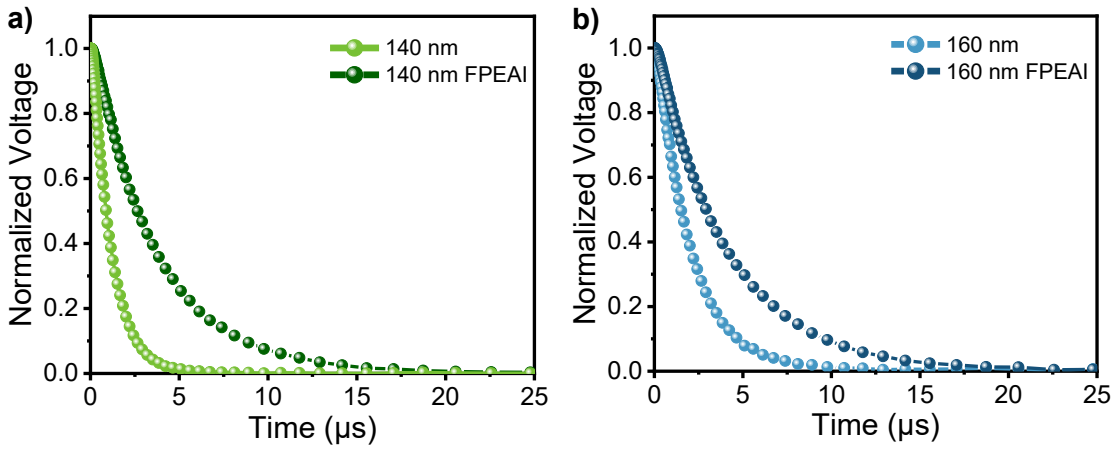

Figure 32. a,b) Transient photovoltage (TPV) measurements of the passivated and non-passivated devices.

Transient photocurrent (TPC) measurements (**Figures 33**) indicate a modest increase in charge extraction times for FPEAI-treated devices relative to pristine samples. The carrier extraction times increase from 1.04 µs to 1.22 µs for the 140 nm configuration and from 1.07 µs to 1.26 µs for the 160 nm devices upon passivation. This slight prolongation of extraction dynamics can be attributed to the presence of the interfacial 2D perovskite layer, which may introduce a minor energy barrier for charge transport. Nevertheless, these extraction times remain within an optimal range for efficient charge collection, ensuring that the passivation strategy does not compromise device functionality.[93–98]

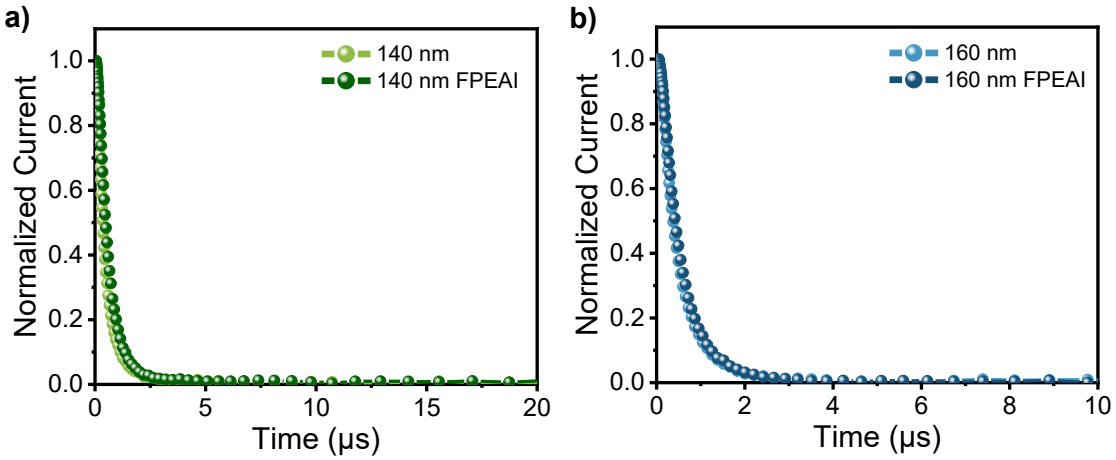

Figure 33. a,b) Transient photocurrent (TPC) of the devices, before and after passivation.

FESEM Imaging

Field-emission scanning electron microscopy (FESEM) analysis was conducted on half-cell structures (glass/ITO/MeO-2PACz/perovskite) to examine the morphological changes induced by the passivation treatment. The top-view images presented in **Figure 34** reveal that the 140 nm FPEAI-treated samples display enhanced surface uniformity with minimized defect density and less pronounced grain boundaries, suggesting improved surface coverage.

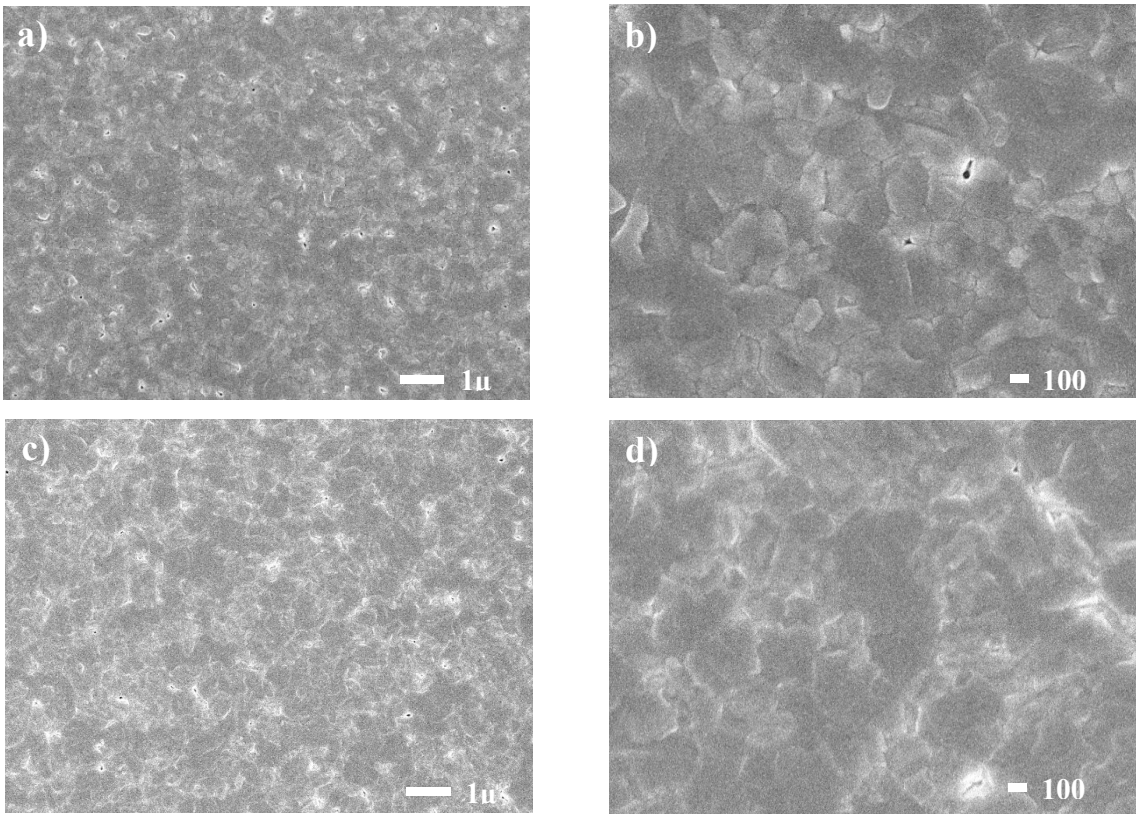

Figure 34. a) Top-view FESEM image of the 140 nm half-cell (magnification 10000x). **b)** zoomed top-view FESEM image of the 140 nm perovskite (magnification 30000x). **c)** Top-view FESEM image of the 140 nm passivated half-cell (magnification 10000x). **b)** zoomed top-view FESEM image of the 140 nm passivated perovskite (magnification 30000x).

FESEM characterization of the 160 nm films with and without FPEAI treatment is presented in **figure 35**. The micrographs reveal a notable decrease in surface defect density for the passivated 160 nm perovskite films. These findings indicate improved surface quality of the perovskite layer following FPEAI treatment.

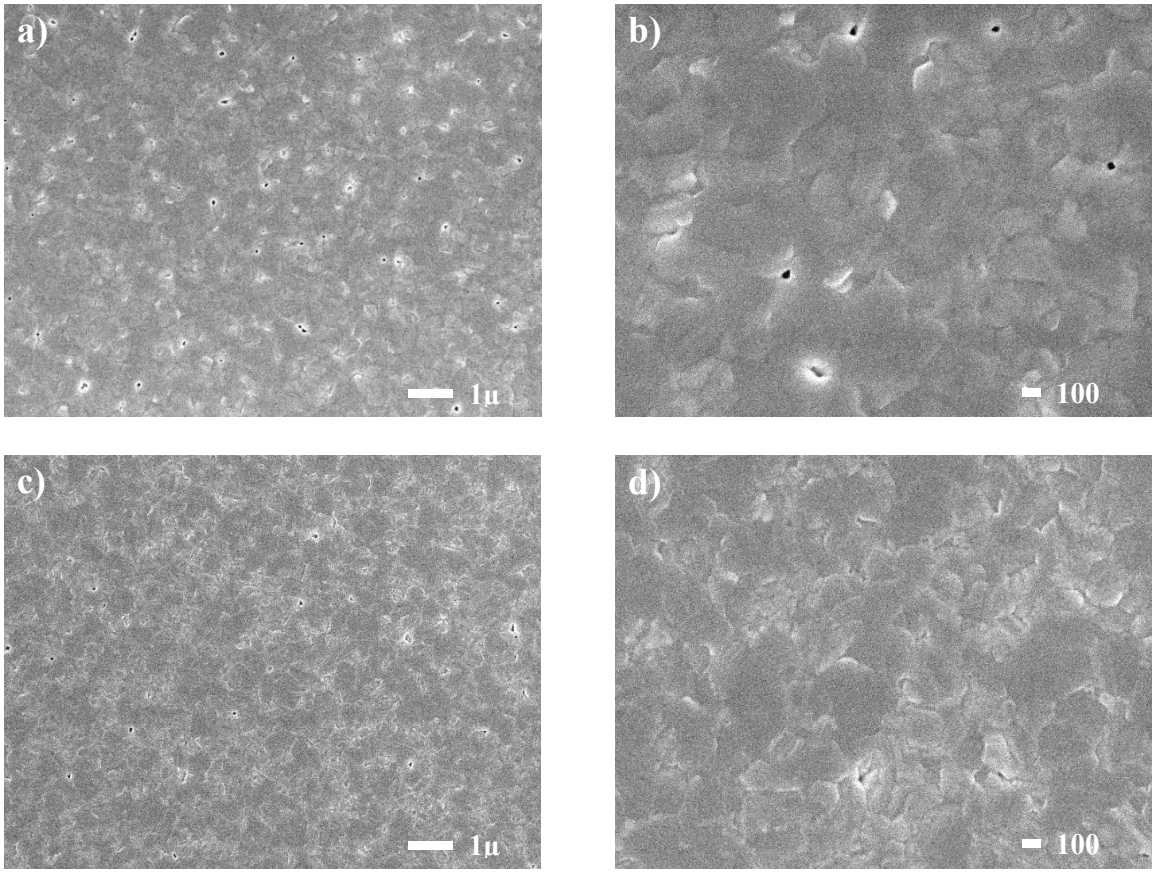

Figure 35. a) Top-view FESEM image of the 160 nm half-cell (magnification 10000x). **b)** zoomed top-view FESEM image of the 160 nm perovskite (magnification 30000x). **c)** Top-view FESEM image of the 160 nm passivated half-cell (magnification 10000x). **b)** zoomed top-view FESEM image of the 160 nm passivated perovskite (magnification 30000x).

3.4 Stability Measurements

To assess the impact of reduced active layer thickness on device stability, comprehensive stability studies were conducted on both passivated and non-passivated semi-transparent solar cells. Two distinct stability protocols were employed to evaluate different degradation mechanisms: shelf-life stability measurements and maximum power point (MPP) tracking under continuous illumination. The shelf-life stability test provides insights into the intrinsic stability of the devices under dark storage conditions, revealing degradation processes related to material decomposition and interface deterioration in the absence of operational stresses. Conversely, MPP tracking under continuous illumination simulates real operational conditions, exposing devices to combined stresses of light, heat, and electrical bias, thereby elucidating photo- and bias-induced degradation pathways. This dual approach enables a comprehensive understanding of how thickness reduction affects both the intrinsic material stability and operational durability of semi-transparent perovskite solar cells, while simultaneously examining the protective role of FPEAI passivation in mitigating degradation mechanisms.

Shelf-Life Stability

A 17-week shelf-life stability test was conducted with samples stored in the dark under nitrogen atmosphere in a glovebox and subjected to periodic performance measurements.

Shelf-life stability results for the 160 nm devices with and without passivation are presented in **Figures 36**. The 80% retention threshold, marked by the dotted line, represents a critical benchmark for device stability. While the best-performing pristine 160 nm devices retained PCE values exceeding 80% of their initial efficiency, the median performance dropped marginally below this threshold after 17 weeks (**Figure 36a**). In contrast, all FPEAI-treated devices demonstrated superior stability, maintaining over 80% of their initial efficiency throughout the entire 17-week testing period, thereby validating the effectiveness

of passivation in enhancing long-term device durability.

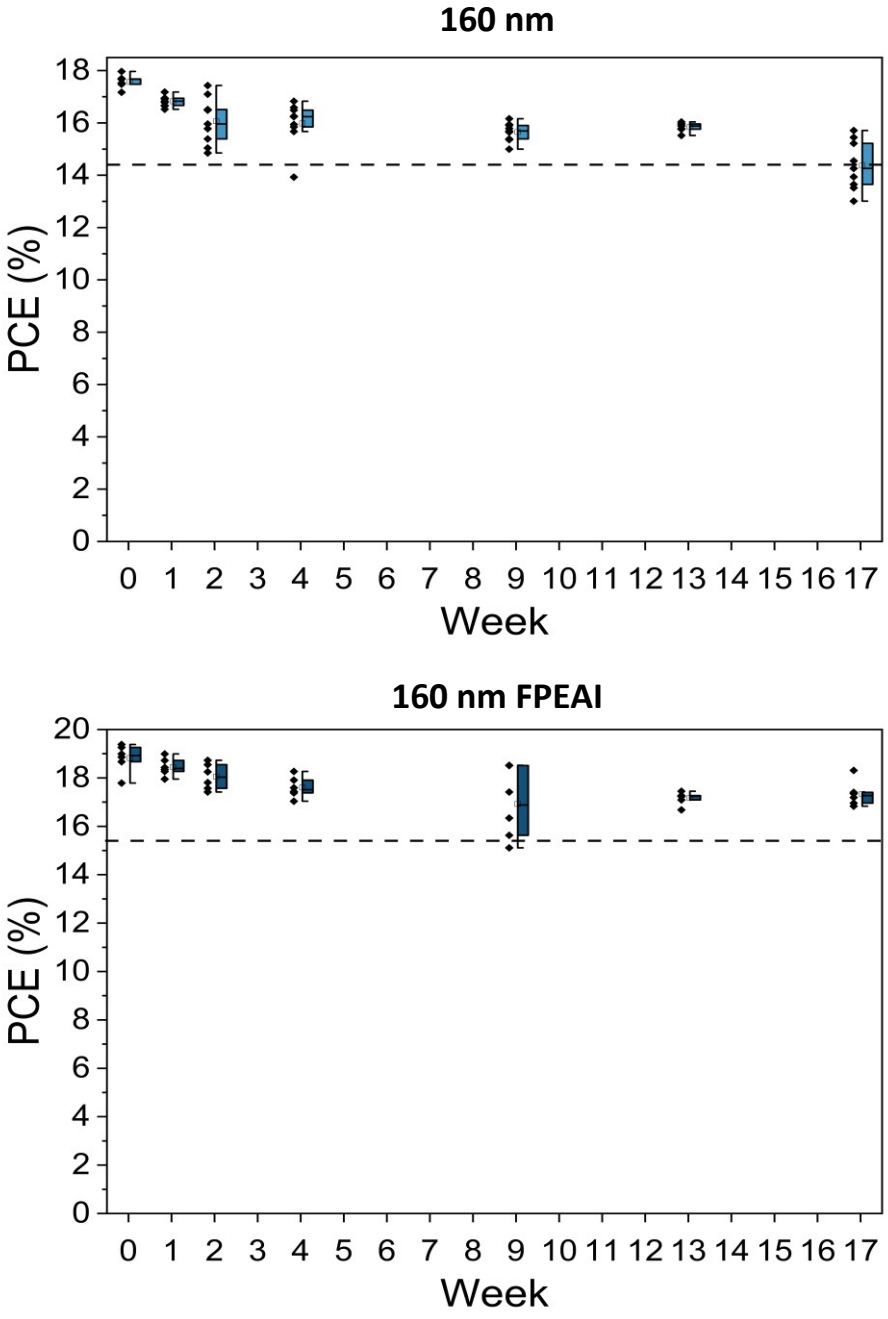

Figure 36. Shelf-life stability test of **a)** 160 nm device and **b)** 160 nm FPEAI devices. The dotted line represents 80% of the initial PCE of the best-performing device.

Regarding the 140 nm devices (**Figures 37**), the limited number of samples and the progressive degradation of metal contacts due to repeated probing further complicated measurements over time. In particular, the alignment between the intact contact areas and the measurement mask was often compromised after

several weeks of testing. Despite these limitations, the general trend suggests that both passivated and non-passivated devices undergo PCE degradation over time. FPEAI-passivated samples exhibit an initial drop below the 80% threshold, with subsequent partial recovery, possibly due to improved interface or contact stabilization over time (**Figure 37b**). The non-passivated devices, on the other hand, show a more gradual decline, though fluctuations due to contact degradation or measurement variability cannot be ruled out (**Figure 37a**).

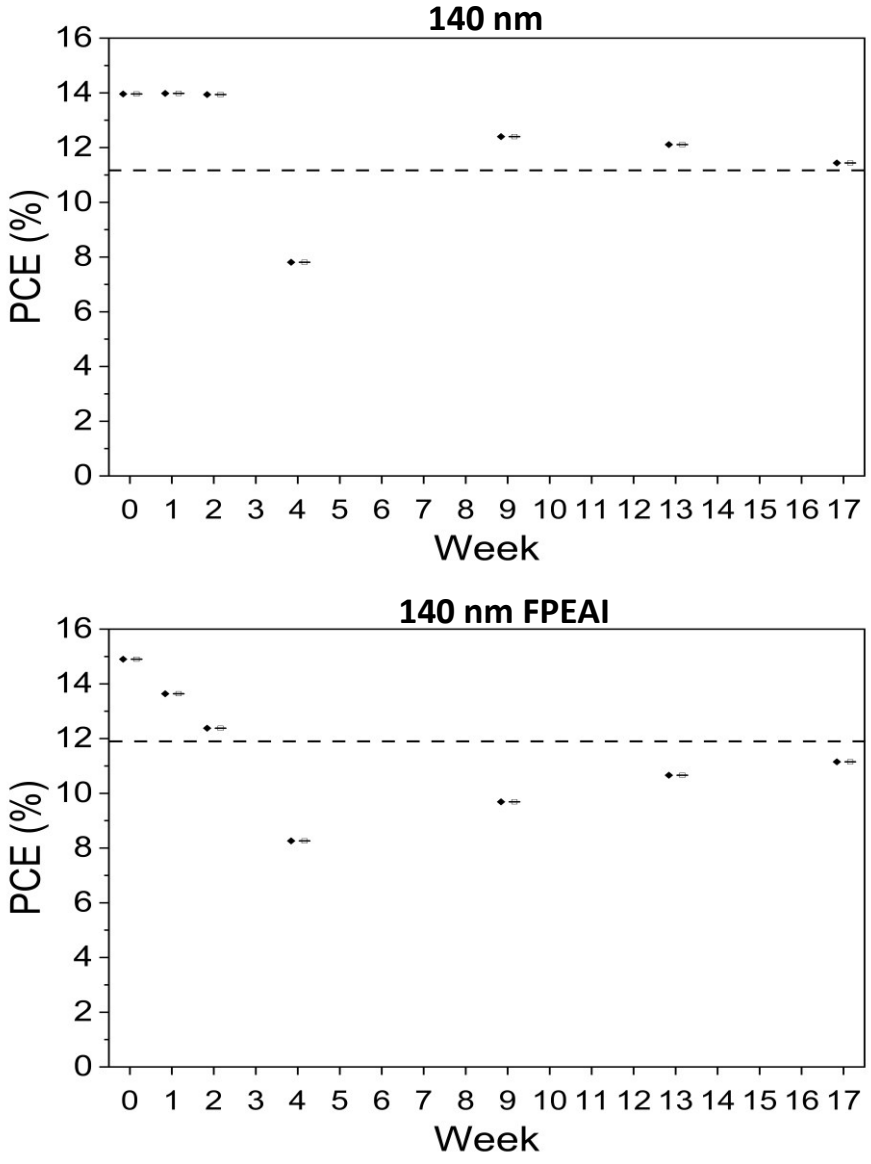

Figure 37. Shelf-life stability test of **a)** 140 nm device and **b)** 140 nm FPEAI devices. The dotted line represents 80% of the initial PCE of the best-performing device.

MPP Tracking Stability

Maximum power point (MPP) tracking experiments were conducted to assess the operational stability of unpassivated devices. The results presented in **Figure 38** demonstrate that both thicknesses exceeded the 80% retention benchmark after 1000 hours of continuous illumination. The 140 nm devices exhibited 88% PCE retention, while the 160 nm devices showed 83% retention relative to their initial efficiencies. These findings, combined with the shelf-life stability data, conclusively demonstrate that thickness reduction from 160 nm to 140 nm does not adversely affect device stability, supporting the viability of thinner active layers for semi-transparent applications.

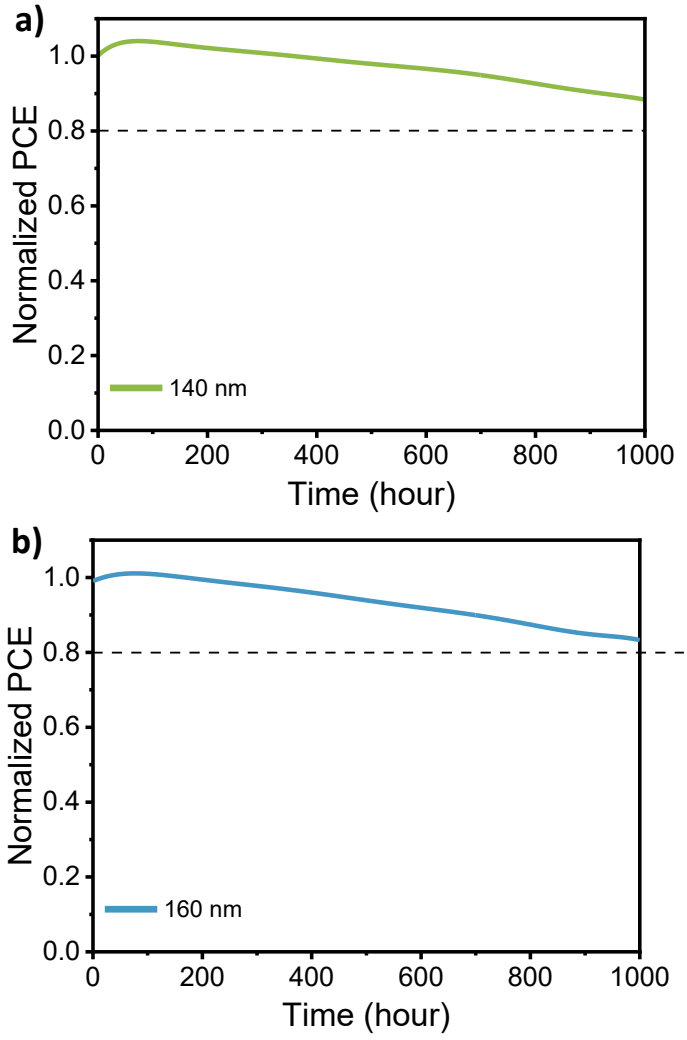

Figure 38. MPP tracking stability test of **a)** 140 nm device and **b)** 160 nm devices. The dotted line represents 80% of the initial PCE.

Chapter 4
Conclusion

This thesis demonstrates a successful approach to fabricating high-performance semi-transparent perovskite solar cells based on FAPbI3 by strategically reducing the active layer thickness and precursor concentration. This straightforward methodology effectively circumvents the phase segregation issues commonly encountered in wide-bandgap bromide-containing perovskites while achieving superior performance compared to low-dimensional perovskite alternatives, all through a simple adjustment of processing parameters.

The pristine devices achieved remarkable performance metrics, with the 140 nm configuration delivering an AVT of 25% with a PCE of 16%, while the 160 nm devices attained an AVT of 20% coupled with a PCE of 18%. These results establish an excellent baseline performance for semi-transparent applications without any surface modification.

The implementation of FPEAI surface passivation proved highly effective in enhancing device performance while preserving optical transparency. The AVT values remained unchanged post-treatment, maintaining the desired optical properties, while the photovoltaic parameters experienced substantial improvements. The passivated devices achieved impressive PCE values of 17% for the 140 nm configuration and 19.5% for the 160 nm devices, representing significant enhancements in power conversion efficiency.

Comprehensive optoelectronic characterization provided deep insights into the passivation mechanisms. PL measurements revealed enhanced radiative recombination efficiency, indicating superior surface quality in passivated films. TRPL analysis demonstrated the suppression of fast decay components associated with surface-mediated recombination, with the complete elimination of the ~1 ns component in treated samples. TPV measurements showed extended carrier lifetimes, increasing from 1.13 μs to 3.51 μs for 140 nm devices and from 2.02 μs to 3.76 μs for 160 nm devices, directly correlating with the observed Voc improvements. TPC analysis confirmed that charge extraction remained efficient despite the presence of the 2D passivation layer, with only marginal increases in extraction times that do not compromise device functionality.

Stability assessments validated the robustness of the thickness-reduction

approach. Shelf-life testing over 17 weeks demonstrated that passivated devices exhibited superior stability compared to their pristine counterparts, while MPP tracking under continuous illumination for 1000 hours showed excellent operational stability, with the 140 nm devices retaining 88% of their initial PCE. These results conclusively prove that reducing the active layer thickness does not compromise device stability, addressing a critical concern for commercial viability.

In conclusion, our strategy of employing thickness-optimized FAPbI3 active layers combined with effective surface passivation has proven highly successful in achieving an exceptional trade-off between optical transparency and photovoltaic efficiency. This approach not only delivers state-of-the-art performance but also demonstrates excellent stability, positioning these semi-transparent solar cells as promising candidates for building-integrated photovoltaics and tandem applications.

Chapter 5

References

(1) Lund, P. D. Global Challenges: Energy. *Global Challenges* **2017**, *1* (1), 7–8. https://doi.org/10.1002/GCH2.1001.

(2) Destouni, G.; Frank, H. Renewable Energy. https://doi.org/10.1007/s13280-010-0059-7.

(3) Sotnyk, I.; Kurbatova, T.; Kubatko, O.; Prokopenko, O.; Prause, G.; Kovalenko, Y.; Trypolska, G.; Pysmenna, U. Energy Security Assessment of Emerging Economies under Global and Local Challenges. *Energies 2021, Vol. 14, Page 5860* **2021**, *14* (18), 5860. https://doi.org/10.3390/EN14185860.

(4) Energy Agency, I. *World Energy Outlook 2024*; 2024. www.iea.org/terms.

(5) Obaideen, K.; Olabi, A. G.; Al Swailmeen, Y.; Shehata, N.; Abdelkareem, M. A.; Alami, A. H.; Rodriguez, C.; Sayed, E. T. Solar Energy: Applications, Trends Analysis, Bibliometric Analysis and Research Contribution to Sustainable Development Goals (SDGs). *Sustainability 2023, Vol. 15, Page 1418* **2023**, *15* (2), 1418. https://doi.org/10.3390/SU15021418.

(6) Hossain, F. Global Sustainability in Energy, Building, Infrastructure, Transportation, and Water Technology. *Global Sustainability in Energy, Building, Infrastructure, Transportation, and Water Technology* **2021**, 1–470. https://doi.org/10.1007/978-3-030-62376-0/COVER.

(7) Renewable Energy Agency, I. *RENEWABLE ENERGY STATISTICS 2025 STATISTIQUES D'ÉNERGIE RENOUVELABLE 2025 ESTADÍSTICAS DE ENERGÍA RENOVABLE 2025*; 2025.

(8) *Perovskite photovoltaics: life-cycle assessment of energy and environmental impacts - Energy & Environmental Science (RSC Publishing) DOI:10.1039/C5EE00615E*. https://pubs.rsc.org/en/content/articlehtml/2015/ee/c5ee00615e (accessed 2025-10-05).

(9) Würfel, Peter. Physics of Solar Cells. **2008**.

(10) Swaaij, van. *Solar Energy The Physics and Engineering of Photovoltaic Conversion, Technologies and Systems*.

(11) Alam Khan, K.; Paul, S.; Kamrul Alam Khan, M.; Zobayer, A.; Sifat Hossain, S. A Study on Solar Photovoltaic Conversion. *Article in International Journal of Scientific and Engineering Research* **2013**, *4*.

(12) Chin, V. J.; Salam, Z.; Ishaque, K. Cell Modelling and Model Parameters

Estimation Techniques for Photovoltaic Simulator Application: A Review. *Appl Energy* **2015**, *154*, 500–519. https://doi.org/10.1016/J.APENERGY.2015.05.035.

(13) An Improved Mathematical Model Derivation Based on Circuitry Approach for Crystalline Silicon Photovoltaic Module. https://doi.org/10.1088/1757-899X/1127/1/012020.

(14) Hsieh, H. C.; Hu, C.; Drowley, C. I. A New Method of Analyzing the Short-Circuit Current of Silicon Solar Cells. *IEEE Trans Electron Devices* **1980**, *27* (4), 883–885. https://doi.org/10.1109/T-ED.1980.19951.

(15) *IV Curve | PVEducation*. https://www.pveducation.org/pvcdrom/solar-cell-operation/iv-curve (accessed 2025-10-05).

(16) Shockley, W.; Queisser, H. J. Detailed Balance Limit of Efficiency of P-n Junction Solar Cells. *J Appl Phys* **1961**, *32* (3), 510–519. https://doi.org/10.1063/1.1736034.

(17) Rühle, S. Tabulated Values of the Shockley–Queisser Limit for Single Junction Solar Cells. *Solar Energy* **2016**, *130*, 139–147. https://doi.org/10.1016/J.SOLENER.2016.02.015.

(18) Markvart, T. Shockley: Queisser Detailed Balance Limit after 60 Years. *Wiley Interdiscip Rev Energy Environ* **2022**, *11* (4), e430. https://doi.org/10.1002/WENE.430.

(19) Romeo, A.; Artegiani, E. CdTe-Based Thin Film Solar Cells: Past, Present and Future. *Energies 2021, Vol. 14, Page 1684* **2021**, *14* (6), 1684. https://doi.org/10.3390/EN14061684.

(20) Allouhi, A.; Rehman, S.; Buker, M. S.; Said, Z. Recent Technical Approaches for Improving Energy Efficiency and Sustainability of PV and PV-T Systems: A Comprehensive Review. *Sustainable Energy Technologies and Assessments* **2023**, *56*, 103026. https://doi.org/10.1016/J.SETA.2023.103026.

(21) Ferekides, C. S.; Balasubramanian, U.; Mamazza, R.; Viswanathan, V.; Zhao, H.; Morel, D. L. CdTe Thin Film Solar Cells: Device and Technology Issues. *Solar Energy* **2004**, *77* (6), 823–830. https://doi.org/10.1016/J.SOLENER.2004.05.023.

(22) *Best Research-Cell Efficiency Chart | Photovoltaic Research | NREL*. https://www.nrel.gov/pv/cell-efficiency.

(23) Keller, J.; Kiselman, K.; Donzel-Gargand, O.; Martin, N. M.; Babucci, M.; Lundberg, O.; Wallin, E.; Stolt, L.; Edoff, M. High-Concentration Silver Alloying and Steep Back-Contact Gallium Grading Enabling Copper Indium

Gallium Selenide Solar Cell with 23.6% Efficiency. *Nat Energy* **2024**, *9* (4), 467–478. https://doi.org/10.1038/S41560-024-01472-3;SUBJMETA.

(24) Pettersson, J.; Torndahl, T.; Platzer-Bjorkman, C.; Hultqvist, A.; Edoff, M. The Influence of Absorber Thickness on Cu(In,Ga)Se2 Solar Cells with Different Buffer Layers. *IEEE J Photovolt* **2013**, *3* (4), 1376–1382. https://doi.org/10.1109/JPHOTOV.2013.2276030.

(25) Hölscher, T.; Placidi, M.; Becerril-Romero, I.; Fonoll-Rubio, R.; Izquierdo-Roca, V.; Thomere, A.; Bailo, E.; Schneider, T.; Kempa, H.; Scheer, R.; Pérez-Rodríguez, A. Effects of ITO Based Back Contacts on Cu(In,Ga)Se2 Thin Films, Solar Cells, and Mini-Modules Relevant for Semi-Transparent Building Integrated Photovoltaics. *Solar Energy Materials and Solar Cells* **2023**, *251*, 112169. https://doi.org/10.1016/J.SOLMAT.2022.112169.

(26) *CIGS Solar Cells Overview | PVEducation*. https://www.pveducation.org/pvcdrom/cigs-solar-cells-overview.

(27) Yuan, S.; Luo, W.; Xie, M.; Peng, H. Progress in Research on Organic Photovoltaic Acceptor Materials. *RSC Adv* **2025**, *15* (4), 2470–2489. https://doi.org/10.1039/D4RA08370A.

(28) Xu, C.; Zhao, Z.; Yang, K.; Niu, L.; Ma, X.; Zhou, Z.; Zhang, X.; Zhang, F. Recent Progress in All-Small-Molecule Organic Photovoltaics. *J Mater Chem A Mater* **2022**, *10* (12), 6291–6329. https://doi.org/10.1039/D1TA10581G.

(29) Yu, X.; Yang, S.; Shao, Z.; Xie, L.; Wang, Z.; Ding, P.; Liu, T.; Wu, J.; Cao, X.; Zhu, J.; Chen, F.; Chen, G.; Yang, D.; Ge, Z. Rational Molecular Design of Guest Acceptor for Organic Solar Cells with 20.2% Efficiency. *Sci China Chem* **2025**, 1–8. https://doi.org/10.1007/S11426-025-2723-9/METRICS.

(30) Ding, P.; Yang, D.; Yang, S.; Ge, Z. Stability of Organic Solar Cells: Toward Commercial Applications. *Chem Soc Rev* **2024**, *53* (5), 2350–2387. https://doi.org/10.1039/D3CS00492A.

(31) Ansari, M. A.; Ciampi, G.; Sibilio, S. Novel Materials for Semi-Transparent Organic Solar Cells. *Energies 2024, Vol. 17, Page 333* **2024**, *17* (2), 333. https://doi.org/10.3390/EN17020333.

(32) Ma, B.; Yan, Y.; Wu, M.; Li, S.; Ru, M.; Xu, Z.; Zhao, W.; Ma, B.; Yan, Y.; Wu, M.; Ru, M.; Xu, Z.; Zhao, W.; Li, S. Sustainable Solution Processing Toward High-Efficiency Organic Solar Cells: A Comprehensive Review of Materials, Strategies, and Applications. *Adv Funct Mater* **2025**, *35* (3), 2413814. https://doi.org/10.1002/ADFM.202413814.

(33) Bularka, S.; Vajda, M.; Ilies, E.; Ricman, R.; Marinca, M.; Miclau, M.;

Gontean, A.; Ursu, D. Photovoltaic Tiles for the Wavelength-Selective Greenhouse: Exploring Yellow and Green Dye-Sensitized Solar Cells in Outdoor Conditions. *Applied Sciences 2024, Vol. 14, Page 1957* **2024**, *14* (5), 1957. https://doi.org/10.3390/APP14051957.

(34) Ursu, D.; Vajda, M.; Miclau, M. Highly Efficient Dye-Sensitized Solar Cells for Wavelength-Selective Greenhouse: A Promising Agrivoltaic System. *Int J Energy Res* **2022**, *46* (13), 18550–18561. https://doi.org/10.1002/ER.8469.

(35) Mikhailov, M. S.; Gudim, N. S.; Mikhalchenko, L. V.; Knysh, M. I.; Knyazeva, E. A.; Rakitin, O. A. Dye-Sensitized Solar Cells Based on D—A—π—A′ Structures with a 4H-Cyclopenta[2,1-b:3,4-B′]Dithiophene Fragment Containing Branched Alkyl Groups. *Russian Chemical Bulletin* **2024**, *73* (8), 2199–2210. https://doi.org/10.1007/S11172-024-4341-4/METRICS.

(36) Prajapat, K.; Dhonde, M.; Sahu, K.; Bhojane, P.; Murty, V. V. S.; Shirage, P. M. The Evolution of Organic Materials for Efficient Dye-Sensitized Solar Cells. *Journal of Photochemistry and Photobiology C: Photochemistry Reviews* **2023**, *55*, 100586. https://doi.org/10.1016/J.JPHOTOCHEMREV.2023.100586.

(37) Alsharif, S. A. Nanograss-Assembled NiCo2S4 as an Efficient Platinum-Free Counter Electrode for Dye-Sensitized Solar Cell. *Nanomaterials* **2023**, *13* (21), 2896. https://doi.org/10.3390/NANO13212896/S1.

(38) Orhan, E.; Gökçen, M.; Taran, S. Synthesis of Benzimidazole Moiety Heteroleptic Ruthenium Complex and Use as Sensitizer in Dye-Sensitized Solar Cells. *Appl Phys A Mater Sci Process* **2021**, *127* (12). https://doi.org/10.1007/S00339-021-05080-W.

(39) Chang, W.-C.; Chen, H.-S.; Li, T.-Y.; Hsu, N.-M.; Tingare, Y. S.; Li, C.-Y.; Liu, Y.-C.; Su, C.; Li, W.-R.; Chang, W.; Li, T.; Hsu, N.; Tingare, Y. S.; Li, C.; Li, W.; Chen, H.; Liu, Y.; Su, C.; Fang, H. A. Highly Efficient N-Heterocyclic Carbene/Pyridine-Based Ruthenium Sensitizers: Complexes for Dye-Sensitized Solar Cells. *Angewandte Chemie* **2010**, *122* (44), 8337–8340. https://doi.org/10.1002/ANGE.201001628.

(40) Sen, A.; Groß, A. Promising Sensitizers for Dye Sensitized Solar Cells: A Comparison of Ru(II) with Other Earth's Scarce and Abundant Metal Polypyridine Complexes. *Int J Quantum Chem* **2019**, *119* (16), e25963. https://doi.org/10.1002/QUA.25963.

(41) Boden, P.; Di Martino-Fumo, P.; Bens, T.; Steiger, S.; Albold, U.; Niedner-Schatteburg, G.; Gerhards, M.; Sarkar, B.; Di Martino-Fumo, P.; Steiger, S.; Niedner-Schatteburg, G.; Gerhards, M.; Bens, T.; Sarkar, B.; Albold, U.

NIR-Emissive Chromium(0), Molybdenum(0), and Tungsten(0) Complexes in the Solid State at Room Temperature. *Chemistry – A European Journal* **2021**, *27* (51), 12959–12964. https://doi.org/10.1002/CHEM.202102208.

(42) Wegeberg, C.; Häussinger, D.; Wenger, O. S. Pyrene-Decoration of a Chromium(0) Tris(Diisocyanide) Enhances Excited State Delocalization: A Strategy to Improve the Photoluminescence of 3d6 Metal Complexes. *J Am Chem Soc* **2021**, *143* (38), 15800–15811. https://doi.org/10.1021/JACS.1C07345.

(43) Abdelaaziz, A.; Bouzzine, S. M.; Hamidi, M.; El-Shishtawy, R. M. Newly Designed Triazatruxene-Based Dye-Sensitized Solar Cells Containing Different Benzothiazine π-Linkers: Geometric, Optoelectronic, Charge Transfer Properties, and Cyanoacrylic Acid versus Benzoic Acid. *Comput Theor Chem* **2023**, *1224*, 114127. https://doi.org/10.1016/J.COMPTC.2023.114127.

(44) Hinsch, A.; Kroon, J. M.; Kern, R.; Uhlendorf, I.; Holzbock, J.; Meyer, A.; Ferber, J. Long-Term Stability of Dye-Sensitised Solar Cells. *Progress in Photovoltaics: Research and Applications* **2001**, *9* (6), 425–438. https://doi.org/10.1002/PIP.397.

(45) Travis, W.; Glover, E. N. K.; Bronstein, H.; Scanlon, D. O.; Palgrave, R. G. On the Application of the Tolerance Factor to Inorganic and Hybrid Halide Perovskites: A Revised System. *Chem Sci* **2016**, *7* (7), 4548–4556. https://doi.org/10.1039/C5SC04845A.

(46) Dai, T.; Cao, Q.; Yang, L.; Aldamasy, M. H.; Li, M.; Liang, Q.; Lu, H.; Dong, Y.; Yang, Y. Strategies for High-Performance Large-Area Perovskite Solar Cells toward Commercialization. *Crystals 2021, Vol. 11, Page 295* **2021**, *11* (3), 295. https://doi.org/10.3390/CRYST11030295.

(47) Sharif, R.; Khalid, A.; Ahmad, S. W.; Rehman, A.; Qutab, H. G.; Akhtar, H. H.; Mahmood, K.; Afzal, S.; Saleem, F. A Comprehensive Review of the Current Progresses and Material Advances in Perovskite Solar Cells. *Nanoscale Adv* **2023**, *5* (15), 3803–3833. https://doi.org/10.1039/D3NA00319A.

(48) Goetz, K. P.; Taylor, A. D.; Paulus, F.; Vaynzof, Y.; Goetz, K. P.; Taylor, A. D.; Paulus, F.; Vaynzof, Y. Shining Light on the Photoluminescence Properties of Metal Halide Perovskites. *Adv Funct Mater* **2020**, *30* (23), 1910004. https://doi.org/10.1002/ADFM.201910004.

(49) Bati, A. S. R.; Zhong, Y. L.; Burn, P. L.; Nazeeruddin, M. K.; Shaw, P. E.; Batmunkh, M. Next-Generation Applications for Integrated Perovskite Solar Cells. *Commun Mater* **2023**, *4* (1), 1–24. https://doi.org/10.1038/S43246-

022-00325-4;SUBJMETA.

(50) Olaleru, S. A.; Kirui, J. K.; Wamwangi, D.; Roro, K. T.; Mwakikunga, B. Perovskite Solar Cells: The New Epoch in Photovoltaics. *Solar Energy* **2020**, *196*, 295–309. https://doi.org/10.1016/J.SOLENER.2019.12.025.

(51) Faini, F.; Larini, V.; Scardina, A.; Grancini, G. Hybrid Halide Perovskites, a Game Changer for Future Solar Energy? *MRS Bull* **2024**, *49* (10), 1059–1069. https://doi.org/10.1557/S43577-024-00784-9/FIGURES/7.

(52) Chen, J.; Park, N. G. Causes and Solutions of Recombination in Perovskite Solar Cells. *Advanced Materials* **2019**, *31* (47), 1803019. https://doi.org/10.1002/ADMA.201803019.

(53) Wang, F.; Cao, Y.; Chen, C.; Chen, Q.; Wu, X.; Li, X.; Qin, T.; Huang, W.; Wang, F.; Cao, Y.; Chen, C.; Chen, Q.; Qin, T.; Huang, W.; Wu, X.; Li, X. Materials toward the Upscaling of Perovskite Solar Cells: Progress, Challenges, and Strategies. *Adv Funct Mater* **2018**, *28* (52), 1803753. https://doi.org/10.1002/ADFM.201803753.

(54) Traverse, C. J.; Pandey, R.; Barr, M. C.; Lunt, R. R. Emergence of Highly Transparent Photovoltaics for Distributed Applications. *Nat Energy* **2017**, *2* (11), 849–860. https://doi.org/10.1038/S41560-017-0016-9;SUBJMETA.

(55) Xu, C.; Chen, Y.; Zhao, Z.; Yang, B.; Suo, J.; Ba, K.; Tarasov, A.; Wu, Y.; Lian, X.; Luo, M.; Zhan, Y.; Chen, Y.; Gao, J.; Mo, X.; Choy, W. C. H.; Wang, J.; Zhang, H.; Chu, J. Semi-Transparent Photovoltaics. *Energy Environ Sci* **2025**, *18* (5), 2095–2135. https://doi.org/10.1039/D4EE04209C.

(56) Sheng, C.; Shi, Y.; Li, Y.; Wang, W.; Zhou, W.; Chen, C.; Zhang, N.; Ran, J.; Stathatos, E.; Yang, B. Semi-Transparent Colored Solar Cells for Agrivoltaics Ecosystem Applications. *Adv Sustain Syst* **2025**, *9* (5), 2401059. https://doi.org/10.1002/ADSU.202401059.

(57) Lee, K.; Um, H.-D.; Choi, D.; Park, J.; Kim, N.; Kim, H.; Seo, K. The Development of Transparent Photovoltaics. *Cell Rep Phys Sci* **2020**, *1*, 100143. https://doi.org/10.1016/j.xcrp.2020.100143.

(58) Kumar, P.; You, S.; Vomiero, A. Recent Progress in Materials and Device Design for Semitransparent Photovoltaic Technologies. *Adv Energy Mater* **2023**, *13* (39), 2301555. https://doi.org/10.1002/AENM.202301555.

(59) Zhou, Z.; Yuan, Z.; Yin, Z.; Xue, Q.; Li, N.; Huang, F. Progress of Semitransparent Emerging Photovoltaics for Building Integrated Applications. *Green Energy & Environment* **2024**, *9* (6), 992–1015. https://doi.org/10.1016/J.GEE.2023.05.006.

(60) Li, Y.; Zheng, D.; Li, J.; Li, Z.; Liu, S.; Peng, L.; Yang, D. Translucent

Solar Power for Potential Future Implementations. *J Mater Chem A Mater* **2024**, *12* (33), 21605–21625. https://doi.org/10.1039/D4TA03542A.

(61) Kwon, H.-C.; Kim, A.; Lee, H.; Lee, D.; Jeong, S.; Moon, J.; Kwon, H.; Kim, A.; Lee, H.; Lee, D.; Moon, J.; Jeong, S. Parallelized Nanopillar Perovskites for Semitransparent Solar Cells Using an Anodized Aluminum Oxide Scaffold. *Adv Energy Mater* **2016**, *6* (20), 1601055. https://doi.org/10.1002/AENM.201601055.

(62) Hörantner, M. T.; Zhang, W.; Saliba, M.; Wojciechowski, K.; Snaith, H. J. Templated Microstructural Growth of Perovskite Thin Films via Colloidal Monolayer Lithography. *Energy Environ Sci* **2015**, *8* (7), 2041–2047. https://doi.org/10.1039/C5EE01169H.

(63) Zhang, L.; Hörantner, M. T.; Zhang, W.; Yan, Q.; Snaith, H. J. Near-Neutral-Colored Semitransparent Perovskite Films Using a Combination of Colloidal Self-Assembly and Plasma Etching. *Solar Energy Materials and Solar Cells* **2017**, *160*, 193–202. https://doi.org/10.1016/J.SOLMAT.2016.10.035.

(64) Eperon, G. E.; Burlakov, V. M.; Goriely, A.; Snaith, H. J. Neutral Color Semitransparent Microstructured Perovskite Solar Cells. *ACS Nano* **2013**, *8* (1), 591–598. https://doi.org/10.1021/NN4052309.

(65) Heo, J. H.; Han, J.; Shin, D. H.; Im, S. H. Highly Stable Semi-Transparent CH3NH3PbI3 Sandwich Type Perovskite Solar Sub-Module with Neutral Color. *Mater Today Energy* **2017**, *5*, 280–286. https://doi.org/10.1016/J.MTENER.2017.07.009.

(66) Della Gaspera, E.; Peng, Y.; Hou, Q.; Spiccia, L.; Bach, U.; Jasieniak, J. J.; Cheng, Y. B. Ultra-Thin High Efficiency Semitransparent Perovskite Solar Cells. *Nano Energy* **2015**, *13*, 249–257. https://doi.org/10.1016/J.NANOEN.2015.02.028.

(67) Upama, M. B.; Mahmud, M. A.; Yi, H.; Elumalai, N. K.; Conibeer, G.; Wang, D.; Xu, C.; Uddin, A. Low-Temperature Processed Efficient and Colourful Semitransparent Perovskite Solar Cells for Building Integration and Tandem Applications. *Org Electron* **2019**, *65*, 401–411. https://doi.org/10.1016/J.ORGEL.2018.11.037.

(68) Yu, J. C.; Sun, J.; Chandrasekaran, N.; Dunn, C. J.; Chesman, A. S. R.; Jasieniak, J. J. Semi-Transparent Perovskite Solar Cells with a Cross-Linked Hole Transport Layer. *Nano Energy* **2020**, *71*, 104635. https://doi.org/10.1016/J.NANOEN.2020.104635.

(69) Woong Jung, J.; Chueh, C.-C.; K-Y Jen, A.; Jung, J. W.; Chueh, C.; K-Y

Jen, A. High-Performance Semitransparent Perovskite Solar Cells with 10% Power Conversion Efficiency and 25% Average Visible Transmittance Based on Transparent CuSCN as the Hole-Transporting Material. *Adv Energy Mater* **2015**, *5* (17), 1500486. https://doi.org/10.1002/AENM.201500486.

(70) Bag, A.; Radhakrishnan, R.; Nekovei, R.; Jeyakumar, R. Effect of Absorber Layer, Hole Transport Layer Thicknesses, and Its Doping Density on the Performance of Perovskite Solar Cells by Device Simulation. *Solar Energy* **2020**, *196*, 177–182. https://doi.org/10.1016/J.SOLENER.2019.12.014.

(71) Beal, R. E.; Slotcavage, D. J.; Leijtens, T.; Bowring, A. R.; Belisle, R. A.; Nguyen, W. H.; Burkhard, G. F.; Hoke, E. T.; McGehee, M. D. Cesium Lead Halide Perovskites with Improved Stability for Tandem Solar Cells. *Journal of Physical Chemistry Letters* **2016**, *7* (5), 746–751. https://doi.org/10.1021/ACS.JPCLETT.6B00002.

(72) Jesper Jacobsson, T.; Correa-Baena, J. P.; Pazoki, M.; Saliba, M.; Schenk, K.; Grätzel, M.; Hagfeldt, A. Exploration of the Compositional Space for Mixed Lead Halogen Perovskites for High Efficiency Solar Cells. *Energy Environ Sci* **2016**, *9* (5), 1706–1724. https://doi.org/10.1039/C6EE00030D.

(73) Mei, J.; Yan, F. Recent Advances in Wide-Bandgap Perovskite Solar Cells. *Advanced Materials* **2025**, 2418622. https://doi.org/10.1002/ADMA.202418622.

(74) Xu, F.; Zhang, M.; Li, Z.; Yang, X.; Zhu, R.; Xu, F.; Yang, X.; Zhu, R.; Zhang, M.; Li, Z. Challenges and Perspectives toward Future Wide-Bandgap Mixed-Halide Perovskite Photovoltaics. *Adv Energy Mater* **2023**, *13* (13), 2203911. https://doi.org/10.1002/AENM.202203911.

(75) Grancini, G.; Nazeeruddin, M. K. Dimensional Tailoring of Hybrid Perovskites for Photovoltaics. *Nat Rev Mater* **2019**, *4* (1), 4–22. https://doi.org/10.1038/S41578-018-0065-0;SUBJMETA.

(76) Zanetta, A.; Andaji-Garmaroudi, Z.; Pirota, V.; Pica, G.; Kosasih, F. U.; Gouda, L.; Frohna, K.; Ducati, C.; Doria, F.; Stranks, S. D.; Grancini, G.; Zanetta, A.; Andaji-Garmaroudi, Z.; Pirota, V.; Pica, G.; Gouda, L.; Doria, F.; Grancini, G.; Frohna, K.; Stranks, S. D.; Kosasih, F. U.; Ducati, C. Manipulating Color Emission in 2D Hybrid Perovskites by Fine Tuning Halide Segregation: A Transparent Green Emitter. *Advanced Materials* **2022**, *34* (1), 2105942. https://doi.org/10.1002/ADMA.202105942.

(77) Li, X.; Hoffman, J. M.; Kanatzidis, M. G. The 2D Halide Perovskite Rulebook: How the Spacer Influences Everything from the Structure to Optoelectronic Device Efficiency. *Chem Rev* **2021**, *121* (4), 2230–2291.

https://doi.org/10.1021/ACS.CHEMREV.0C01006.

(78) Zanetta, A.; Larini, V.; Vikram; Toniolo, F.; Vishal, B.; Elmestekawy, K. A.; Du, J.; Scardina, A.; Faini, F.; Pica, G.; Pirota, V.; Pitaro, M.; Marras, S.; Ding, C.; Yildirim, B. K.; Babics, M.; Ugur, E.; Aydin, E.; Ma, C. Q.; Doria, F.; Loi, M. A.; De Bastiani, M.; Herz, L. M.; Portale, G.; De Wolf, S.; Islam, M. S.; Grancini, G. Vertically Oriented Low-Dimensional Perovskites for High-Efficiency Wide Band Gap Perovskite Solar Cells. *Nature Communications* **2024**, *15* (1), 1–10. https://doi.org/10.1038/S41467-024-53339-6;TECHMETA.

(79) Fortunato, E.; Ginley, D.; Hosono, H.; Paine, D. C. Transparent Conducting Oxides for Photovoltaics. *MRS Bull* **2007**, *32* (3), 242–247. https://doi.org/10.1557/MRS2007.29/METRICS.

(80) Lewis, B. G.; Paine, D. C. Applications and Processing of Transparent Conducting Oxides. *MRS Bull* **2000**, *25* (8), 22–27. https://doi.org/10.1557/MRS2000.147/METRICS.

(81) Li, M.; Liu, M.; Qi, F.; Lin, F. R.; Jen, A. K. Y. Self-Assembled Monolayers for Interfacial Engineering in Solution-Processed Thin-Film Electronic Devices: Design, Fabrication, and Applications. *Chem Rev* **2024**, *124* (5), 2138–2204. https://doi.org/10.1021/ACS.CHEMREV.3C00396.

(82) Wei, Y.; Lu, F.; Ai, X.; Lei, J.; Bai, Y.; Wei, Z.; Chen, Z. Towards High-Performance Inverted Mesoporous Perovskite Solar Cell by Using Bathocuproine (BCP). *Molecules 2024, Vol. 29, Page 4009* **2024**, *29* (17), 4009. https://doi.org/10.3390/MOLECULES29174009.

(83) Kistler, S. F. .; Schweizer, P. M. . *Liquid Film Coating : Scientific Principles and Their Technological Implications*; Springer Science & Business Media, B.V., 2012.

(84) Meyerhofer, D. Characteristics of Resist Films Produced by Spinning. *J Appl Phys* **1978**, *49* (7), 3993–3997. https://doi.org/10.1063/1.325357.

(85) Nečas, D.; Klapetek, P. Gwyddion: An Open-Source Software for SPM Data Analysis. *Central European Journal of Physics* **2012**, *10* (1), 181–188. https://doi.org/10.2478/S11534-011-0096-2/METRICS.

(86) Pica, G.; Bajoni, D.; Grancini, G. A Step beyond in Steady-State and Time-Resolved Electro-Optical Spectroscopy: Demonstration of a Customized Simple, Compact, Low-Cost, Fiber-Based Interferometer System. *Structural Dynamics* **2022**, *9* (1), 11101. https://doi.org/10.1063/4.0000134.

(87) Hierrezuelo-Cardet, P.; Palechor-Ocampo, A. F.; Caram, J.; Ventosinos, F.; Pérez-Del-Rey, D.; Bolink, H. J.; Schmidt, J. A. External Quantum

Efficiency Measurements Used to Study the Stability of Differently Deposited Perovskite Solar Cells. *J Appl Phys* **2020**, *127* (23). https://doi.org/10.1063/5.0011503.

(88) Ragni, M.; Faini, F.; Degani, M.; Cavalli, S.; Postuma, I.; Grancini, G. Machine Learning for Screening and Predicting the Best Surface Modifiers for a Rational Optimization of Efficient Perovskite Solar Cells. *APL Energy* **2024**, *2* (3). https://doi.org/10.1063/5.0214736.

(89) Teale, S.; Degani, M.; Chen, B.; Sargent, E. H.; Grancini, G. Molecular Cation and Low-Dimensional Perovskite Surface Passivation in Perovskite Solar Cells. *Nat Energy* **2024**, *9* (7), 779–792. https://doi.org/10.1038/S41560-024-01529-3;SUBJMETA.

(90) Degani, M.; Pallotta, R.; Pica, G.; Karimipour, M.; Mirabelli, A.; Frohna, K.; Anaya, M.; Xu, T.; Ma, C. Q.; Stranks, S. D.; Cantù, M. L.; Grancini, G. Compositional Gradient of Mixed Halide 2D Perovskite Interface Boosts Outdoor Stability of Highly Efficient Perovskite Solar Cells. *Adv Energy Mater* **2025**, *15* (17), 2404469. https://doi.org/10.1002/AENM.202404469.

(91) Stranks, S. D.; Snaith, H. J. Metal-Halide Perovskites for Photovoltaic and Light-Emitting Devices. *Nat Nanotechnol* **2015**, *10* (5), 391–402. https://doi.org/10.1038/NNANO.2015.90;SUBJMETA.

(92) Wolff, C. M.; Caprioglio, P.; Stolterfoht, M.; Neher, D.; Wolff, C. M.; Caprioglio, P.; Stolterfoht, M.; Neher, D. Nonradiative Recombination in Perovskite Solar Cells: The Role of Interfaces. *Advanced Materials* **2019**, *31* (52), 1902762. https://doi.org/10.1002/ADMA.201902762.

(93) Goetz, K. P.; Taylor, A. D.; Paulus, F.; Vaynzof, Y.; Goetz, K. P.; Taylor, A. D.; Paulus, F.; Vaynzof, Y. Shining Light on the Photoluminescence Properties of Metal Halide Perovskites. *Adv Funct Mater* **2020**, *30* (23), 1910004. https://doi.org/10.1002/ADFM.201910004.

(94) Abudulimu, A.; Fu, S.; Katakumbura, N.; Sun, N.; Carter, S.; Brau, T.; Chen, L.; Rajakaruna, M.; Friedl, J.; Song, Z.; Phillips, A. B.; Heben, M. J.; Yan, Y.; Ellingson, R. J. Enhanced Understanding of Recombination Mechanisms in High-Performance Tin-Lead Perovskite Solar Cells. *Cell Rep Phys Sci* **2025**, *6* (1), 102349. https://doi.org/10.1016/J.XCRP.2024.102349.

(95) Hidayat, R.; Nurunnizar, A. A.; Fariz, A.; Herman; Rosa, E. S.; Shobih; Oizumi, T.; Fujii, A.; Ozaki, M. Revealing the Charge Carrier Kinetics in Perovskite Solar Cells Affected by Mesoscopic Structures and Defect States from Simple Transient Photovoltage Measurements. *Sci Rep* **2020**, *10* (1), 1–13. https://doi.org/10.1038/S41598-020-74603-X;SUBJMETA.

(96) Hsieh, T.-Y.; Pylnev, M.; Palomares, E.; Wei, T.-C.; Hsieh, T.-Y.; Pylnev, M.; Wei, -C T; Palomares, E. Exceptional Long Electron Lifetime in Methylammonium Lead Iodide Perovskite Solar Cell Made from Aqueous Lead Nitrate Precursor. *Adv Funct Mater* **2020**, *30* (10), 1909644. https://doi.org/10.1002/ADFM.201909644.

(97) Shi, J.; Li, Y.; Li, Y.; Li, D.; Luo, Y.; Wu, H.; Meng, Q. From Ultrafast to Ultraslow: Charge-Carrier Dynamics of Perovskite Solar Cells. *Joule* **2018**, *2* (5), 879–901. https://doi.org/10.1016/J.JOULE.2018.04.010.

(98) Cudo, K.; Ollearo, R.; Gelinck, G. H.; Galagan, Y.; Glowienka, D. Quantitative Loss Analysis of Opaque Perovskite Solar Cells Using Transient and Steady-State Characterization. *Phys Rev Appl* **2024**, *22* (5), 054025. https://doi.org/10.1103/PhysRevApplied.22.054025.

(99) *Optimizing I-V Curve Tracing Activities*. https://www.purepower.com/blog/optimizing-iv-curve-tracing-activities (accessed 2025-10-05).

(100) Roslan, N.; Ya'acob, M. E.; Radzi, M. A. M.; Hashimoto, Y.; Jamaludin, D.; Chen, G. Dye Sensitized Solar Cell (DSSC) Greenhouse Shading: New Insights for Solar Radiation Manipulation. *Renewable and Sustainable Energy Reviews* **2018**, *92*, 171–186. https://doi.org/10.1016/J.RSER.2018.04.095.

(101) Bing, J.; Caro, L. G.; Talathi, H. P.; Chang, N. L.; Mckenzie, D. R.; Ho-Baillie, A. W. Y. Perovskite Solar Cells for Building Integrated Photovoltaics—Glazing Applications. *Joule* **2022**, *6* (7), 1446–1474. https://doi.org/10.1016/J.JOULE.2022.06.003.

(102) Ming Koh, T.; Wang, H.; Fong Ng, Y.; Bruno, A.; Mhaisalkar, S.; Mathews, N.; Koh, T. M.; Wang, H.; Ng, Y. F.; Bruno, A.; Mhaisalkar, S.; Mathews, N. Halide Perovskite Solar Cells for Building Integrated Photovoltaics: Transforming Building Façades into Power Generators. *Advanced Materials* **2022**, *34* (25), 2104661. https://doi.org/10.1002/ADMA.202104661.